



## D2.4

# Specification of hardware resources and performance requirements

<b>Project number:</b>	101013425
<b>Project acronym:</b>	<b>REINDEER</b>
<b>Project title:</b>	REsilient INteractive applications through hyper Diversity in Energy Efficient RadioWeaves technology
<b>Project Start Date:</b>	1 <sup>st</sup> January, 2021
<b>Duration:</b>	48 months
<b>Programme:</b>	H2020-ICT-52-2020
<b>Deliverable Type:</b>	Report
<b>Reference Number:</b>	ICT-52-2020 / D2.4 / 1
<b>Reference Number:</b>	ICT-52-2020 / D2.4 / 1
<b>Workpackage:</b>	WP2
<b>Due Date:</b>	Dec 31, 2024 (M48)
<b>Actual Submission Date:</b>	Dec 20, 2024
<b>Responsible Organisation:</b>	Lund University
<b>Editor:</b>	Ove Edfors
<b>Dissemination Level:</b>	PU
<b>Revision:</b>	1
<b>Abstract:</b>	Discussion and analysis of RadioWeaves architecture, including control mechanisms and requirements on analog and digital hardware, leading into energy models for both domains and energy efficiency case studies for both communication and power transfer. Conclusions regarding energy consumption for different deployment/design choices are drawn.
<b>Keywords:</b>	Architecture, control mechanisms, energy models, energy optimization, energy efficiency



The REINDEER project has received funding from the European Union's Horizon 2020 research and innovation programme under grant agreement No 101013425.

## **Editor**

Ove Edfors (ULUND)

## **Contributors**

Gilles Callebaut, Jarne Van Mulders (KU Leuven)

Baktash Behmanesh, Ove Edfors, Emma Fitzgerald, Liang Liu, William Tärneberg, Juan Vidal Alegría (ULUND)

Pål Frenger (EAB)

## **Internal reviewers**

Lieven De Strycker (KU Leuven)

Marion Habernig (Technikon)

## **Disclaimer**

*The information in this document is provided as is, and no guarantee or warranty is given that the information is fit for any particular purpose. The content of this document reflects only the author's view – the European Commission is not responsible for any use that may be made of the information it contains. The users use the information at their sole risk and liability.*

## Executive Summary

This deliverable concludes the RadioWeaves infrastructure hardware studies in WP2 of the REINDEER project. A continuation of earlier results reported in deliverables D2.1–D2.3 [1–3], this one focuses on hardware requirements and resulting energy consumption. Control mechanisms and requirements on both analog and digital hardware components are discussed, together with an overview of synchronization options. Energy models are developed for both analog and digital parts of the hardware, followed by case studies where both communication and energy transfer cases are optimized to establish energy efficiency characteristics. An important conclusion is that, for small indoor scenarios with a limited number of users, the energy requirement of the contact service points (CSPs) are highly critical for the sustainability of a distributed RadioWeaves deployment and centralized solutions may be preferred.

# Contents

<b>1</b>	<b>Introduction</b>	<b>1</b>
<b>2</b>	<b>Targeted capabilities of RadioWeaves</b>	<b>2</b>
2.1	RadioWeaves envisioned capabilities . . . . .	2
2.2	Identified challenges per use case . . . . .	3
<b>3</b>	<b>Control mechanisms, and hardware requirements</b>	<b>5</b>
3.1	Control mechanisms . . . . .	5
3.2	Analysis of hardware requirements . . . . .	6
3.2.1	Radios . . . . .	6
3.2.2	Processing (distributed and central) and associated data exchange between nodes . . . . .	10
3.2.3	Calibration and synchronization . . . . .	17
<b>4</b>	<b>Energy efficiency analysis</b>	<b>20</b>
4.1	Energy efficiency overview . . . . .	20
4.2	Energy consumption models . . . . .	21
4.2.1	Analog blocks . . . . .	22
4.2.2	Digital signal processing . . . . .	23
4.2.3	Data shuffling . . . . .	24
4.3	RadioWeaves case studies . . . . .	24
4.3.1	Optimizing downlink communication considering the total energy consumption . . . . .	24
4.3.2	Optimizing the WPT considering the transmit consumption . . . . .	31
4.3.3	Key Contributions . . . . .	31
4.3.4	System Model . . . . .	31
4.3.5	Optimization Framework . . . . .	31
4.3.6	Evaluation and Results . . . . .	32
4.3.7	Conclusion . . . . .	34
<b>5</b>	<b>Summary</b>	<b>35</b>
	<b>Bibliography</b>	<b>41</b>

## List of Figures

3.1	Example of scalable and distributed processing in a RadioWeave system. . . . .	6
3.2	Distribution of individual radiated power levels for the 84 antennas over multiple timeslots [4]. . . . .	10
3.3	Daisy chain topology. . . . .	12
3.4	Bidirectional chain topology. . . . .	13
3.5	Binary tree topology. . . . .	14
3.6	Square grid topology. . . . .	15
3.7	Node aggregation for square grid topology, where $\mathbf{X} \in \{z_{\text{MRC}}, \mathbf{G}\}$ corresponds to the data to be aggregated. . . . .	16
3.8	Synchronization mechanisms between distributed CSPs using (a) a sync signal and (b) sigma-delta over fiber (SDoF). The sync signal can be either an Ethernet-based or dedicated cabling or over-the-air (OTA) technique, the principle remains that instead of sharing a local oscillator (LO), the phase-locked loop (PLL) is calibrated based on an external sync signal. Used abbreviations: base-band (BB), digital up-converter (DUC), sigma-delta modulator (SDM), optic-to-electrical (O/E). . . . .	19
4.1	High-level block diagram of the RadioWeaves hardware. . . . .	21
4.2	Total power consumption in terms of data rate for different numbers of CSPs and antennas. Each row in the legend corresponds with the same number of total antennas. . . . .	29
4.3	Power consumption in terms of number of federations for different rate requirements. . . . .	30
4.4	Illustration of a distributed wireless power transfer (WPT) system, where several Energy Transmitters (ETs) transmit signals over $M$ antennas to $K$ Energy Receivers (ERs) to charge them over $N$ time slots. In this example, during slot $n$ only ER $k$ is targeted, while at $n + 1$ ER <sub>0</sub> and ER <sub><math>K-1</math></sub> is being charged. . . . .	31
4.5	Total transmit power of all deployed antennas for the coherent and non-coherent system. Initially, with a limited number of antennas, both systems exhibit similar transmit power, when the number of antennas increases, the non-coherent system plateaus, whereas the coherent system continues to improve. . . . .	32
4.6	Simulation (a) and measurement-based (b) cumulative distribution function (CDF) of the received direct current (DC) energy over the full 12-hour window for 2, 8 and 84 antennas. . . . .	33
4.7	The used transmit powers (z-axis) over the full-time window (x-axis) for different number of available antennas (y-axis) in the coherent system. . . . .	34

## List of Tables

3.1	Calibration and Synchronization mechanisms employed in sixth-generation (6G) testbeds. Addressing the calibration issue is indicated by ✓. How well the mechanism can scale with both the geographical dispersion and the number of CSPs in distributed MIMO (D-MIMO) is marked by, ●○○, ●●○ and ●●●. More details regarding the mechanisms can be found in the included references (Ref. column).	18
4.1	Hardware components in RadioWeaves and power/energy consumption model . .	22
4.2	Considered energy consumption model and parameters of the system (Part 1). . .	25
4.3	Considered energy consumption model and parameters of the system (Part 2). . .	25

# Chapter 1

## Introduction

This deliverable constitutes a summary and, in addition, final results and conclusions regarding the RadioWeaves infrastructure developed and addressed in the REINDEER project.

Chapter 2 provides a summary of targeted capabilities of RadioWeaves and discusses challenges identified for each use case. This information is also available in other deliverables, such as [1–3, 5], and in much more detail therein. The summary provided here is to be seen as a brief reminder and a back-drop to the coming chapters.

Chapter 3 gives an quick overview of the RadioWeaves architecture and continues with discussions about various aspects of hardware requirements and design options.

Chapter 4 addresses energy consumption of a RadioWeaves infrastructure, under realistic assumptions and in different scenarios. Energy consumption of both analog and digital hardware is modeled. Finally the entire RadioWeaves systems are modeled and optimized for communication and WPT.

An overall summary is provided in Chapter 5.

## Chapter 2

# Targeted capabilities of RadioWeaves

There is a wide range of capabilities envisioned for a RadioWeaves deployment, as initially outlined in [5] and further discussed in [1]. To set the stage of the coming discussions about hardware resources and performance requirements on individual hardware blocks, this chapter provides a short re-cap of the capabilities envisioned and a high-level discussion on how to achieve each of them. For a more complete description we refer to [5] and [1].

### 2.1 RadioWeaves envisioned capabilities

**Carrier frequency** Four different carrier frequency ranges are anticipated, 900 MHz, 2.4 GHz, 3.8 GHz, and 5+ GHz. Depending on the use case, one or more frequency ranges are of interest. Handling of multiple frequency bands can be done either with wide-band radio frequency (RF) front-ends or a combination of more narrow-band ones for each frequency band.

**Device density** Device densities across use cases span three orders-of-magnitude, from 0.1 to 100 devices/m<sup>2</sup>, depending on use case. The approach to handling device densities span from low-density and high data rates, using spatial multiplex, to high-density and low-data rates, using additional time and frequency multiplex.

**Number of devices and user data rates** The combination of the number of devices and experienced user data rates determine the aggregated data traffic a RadioWeaves infrastructure should be able to handle. Across use cases up to 50 Gbps can be expected.

**Mobility** Mobility is rather limited for RadioWeaves, with maximum mobility set to 10 m/s. Given the frequency ranges addressed, this leads to shortest coherence time of about 3 ms, making reciprocal time division duplexing (TDD) operation possible. Some of the use cases have low number of data bits transmitted per coherence time, which may lead to a large overhead in terms of channel state information (CSI) acquisition.

**Positioning accuracy** For positioning services or positioning-based services, accuracies between 0.1 to 1 m are specified among the use cases. Using time-of-arrival methods for position can be challenging, but exploiting the distributed nature of RadioWeaves opens up for more precise positioning, using spatial properties of the environment.



**End-to-end latency** Low end-to-end latency is one of the most critical and demanding requirements, that has the potential to strongly influence how RadioWeaves is designed and how nodes in the infrastructure can cooperate to process and deliver services. Major contributors to end-to-end latency is centralized baseband processing of many users and TDD frame structure, while propagation delays and processing-data exchange between RadioWeaves nodes are typically minor contributors.

**Reliability** Reliability is expressed in terms of *packet loss probability* and range from  $10^{-2}$  to  $10^{-6}$ . These levels of reliability are not difficult to achieve, except for cases where tight latency requirements prevent the use of re-transmissions. Preemptive measures include well distributed CSPs, co-processing of signals from multiple CSPs and the use of environment learning strategies.

**Traffic-volume density** Traffic-volume density is expressed in terms of Mbps/m<sup>2</sup> and ranges between 0.1 and 100 across use cases. For a given use case, a RadioWeaves infrastructure can be deployed densely enough to handle the required traffic-volumes.

**Power density** Requirements on power density applies to use cases where harvesting is a primary, or optional, source of energy for providing necessary functionality of devices. To meet requirements we may increase transmit power from CSPs, use coherent transmission to achieve array gains (from one or more CSPs), and/or densify the RadioWeaves infrastructure to reduce propagation distances.

## 2.2 Identified challenges per use case

In addition to the above, the project initially identified the following per-use-case challenges:

### 1. Augmented reality for sport events

High aggregate data rate to be supported by RadioWeaves, with corresponding high requirements on the RadioWeaves X-haul, including both front-haul and back-haul connections.

### 2. Real-time digital twins in manufacturing

Positioning accuracy at wavelength scale puts localization/positioning performance in focus. Very tight requirements on latency, together with a large number of simultaneous devices, implies high demands on RadioWeaves spatial multiplexing capacity.

### 3. Patient monitoring with in-body and wearable sensors

Energy-neutral operation of devices with high power density requirement makes wireless power transfer a critical RadioWeaves service.

### 4. Human and robot co-working

Very low latency, combined with high reliability, is a well known and difficult challenge. Despite low per-user data rates, RadioWeaves spatial multiplexing capability and channel hardening will serve this use case well. This puts high demands on synchronization between CSPs.

### 5. **Tracking of goods and real-time inventory**

Very challenging combination of KPI requirements. This use case will have to be given particular attention in the RadioWeaves design, since it stands out in terms of device density, mobility, and positioning accuracy. Some of the requirements can be made less severe by, *e.g.*, selecting an appropriate carrier frequency.

### 6. **Electronic labelling**

A high device density and energy-neutral operation, puts WPT at the center, with relatively low requirements on other KPIs. Low requirements on latency and other KPIs allows for efficient and innovative solutions.

### 7. **Augmented reality for professional applications**

Potentially very high per-user data rates and energy-neutral operation, in combination with tight latency requirement, makes a challenging use case to support.

### 8. **Wander detection and patient finding**

Relatively mild requirements across all KPIs. Energy-neutral operation, leading to relatively high power densities, can influence technical requirements when deployed in, *e.g.* hospital environments.

### 9. **Contact tracing and people tracking in large venues**

The most critical requirement is the large number of devices, while remaining requirements are relatively mild.

### 10. **Position tracking of robots and UVs**

Potentially very high device density will make it necessary to use a high carrier frequency for efficient spatial multiplexing and a combination with other multiple-access techniques when spatial multiplexing has reached its limit.

### 11. **Location-based information transfer**

This use case does not stand out in comparison with the rest, with relatively mild requirements across all KPIs.

### 12. **Virtual reality home gaming**

High requirement on user data rates that become less critical when combined with low device densities. Otherwise, relatively low requirements on all KPIs. Deployment in homes point towards low-cost infrastructure.

### 13. **Smart home automation**

High per unit-area device densities, somewhat relaxed by an expected three-dimensional distribution of devices. High positioning accuracy that may be challenging to meet with low-cost home deployments of RadioWeaves.

# Chapter 3

## Control mechanisms, and hardware requirements

In this chapter we first describe in general how a RadioWeaves infrastructure can be controlled, using dynamic federations that adapt to current traffic conditions. This description is followed by an overview of hardware requirements, including analog front ends/radios, distributed processing and calibration and synchronization between nodes.

### 3.1 Control mechanisms

Traffic in realistic networks is very unpredictable and bursty. To effectively operate a RadioWeave system under such conditions the sub-set of service points serving a UE, i.e. the serving federation, needs to be created at the same time scale as the traffic changes. This implies that such federations need to be very dynamic and short lived, just like the majority of traffic sessions are.

An example depicting how processing can be efficiently distributed in a RadioWeave system is depicted in Figure 3.1. The selection of CSPs in each federation can e.g. be based on uplink sounding reference signals (SRSs) from the UEs (depicted by colored circles in the left sub-figure). Each federation has a federation anchor (the colored squares in the right sub-figure) where processing is performed, and each non-anchor SP forwards low level signals to the federation anchor (as indicated by the colored arrows in the right sub-figure). This example depicts uplink transmission. The scheduling of uplink and downlink UEs will impact where in the RadioWeave processing is most efficiently performed. Ideally the co-scheduled UEs should be as distributed as possible over the coverage area to avoid processing and front-haul signal-forwarding bottlenecks.

At any given transmission time interval (TTI), different CSPs and front-haul segments will be active, depending on which UEs that are currently active. The remaining CSPs and front-haul segments should preferably be deactivated and enter low energy consumption sleep modes. This not only reduce operational cost, but it also enables power supply to be distributed over larger distances in the RadioWeaves infrastructure. Assuming that each CSP can have its own dedicated power supply leads to poor scalability, and hence deactivating unused hardware resources is critical for cost efficient installations.

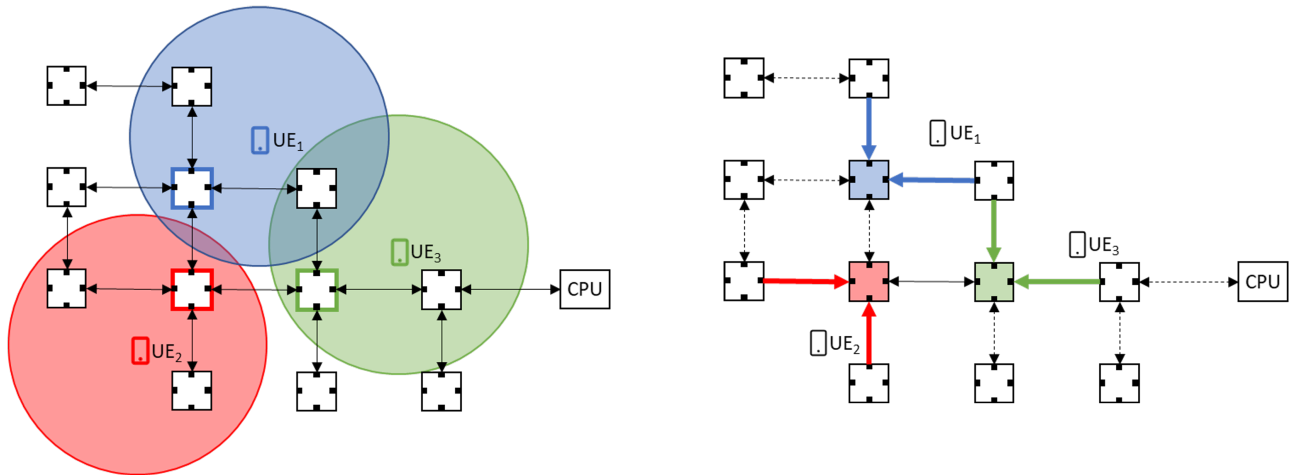


Figure 3.1: Example of scalable and distributed processing in a RadioWeave system.

## 3.2 Analysis of hardware requirements

Designing hardware for RadioWeaves infrastructures requires careful analysis, starting from high-level application and system requirements, which should then be translated into design specifications for hardware. Design space exploration and design choice optimization need to be performed to have a balanced trade-off among, for instance, performance (throughput, latency, gain, linearity, noise figure), power consumption, hardware resource cost, as well as flexibility and scalability. It is difficult, in practice, to include all the aforementioned aspects in this section. Thereby, we have selected the following three topics, which we believe are important and challenging for implementing RadioWeaves infrastructures.

The first subsection focuses on radio hardware for both communication and wireless power transfer. While these two applications may have different requirements for the RF hardware in terms of transmit power, linearity, noise, and coherence, (partial) hardware reuse could potentially be achieved to reduce cost for design, fabrication and infrastructure installation. The second subsection looks into processing aspects, especially the processing scheduling for distributed RadioWeaves architectures. The corresponding challenges include how to keep the cost and power consumption low while meeting the throughput and latency requirements and also providing flexibility and scalability for system adaptation/reconfiguration. The last subsection will discuss time, frequency, and phase synchronization, which is the foundation for RF operations. Different synchronization methods will be discussed, including both off-line and on-line mechanisms, over-the-air and cabled solutions.

### 3.2.1 Radios

Radio front-end designs for D-MIMO systems, especially those with a large total number of antennas as RadioWeaves, has not been addressed in any great detail in literature. In the context of RadioWeaves, there is a potential for re-use of hardware between services providing wireless communication and power transfer. Whether this is possible, or even desirable, depends largely on the use case and deployment details. For this reason we treat communication and power transfer services separately in this description.

### 3.2.1.1 Communication

It is well established that systems operating coherently with many antennas benefit from array gain and can operate with less transmit power than wireless systems delivering the same level of service without coherent operation or with fewer antennas. This translates to a substantially lower requirement on transmit power from each antenna element/transmitter (TX) unit. With  $N$  coherently operating antenna elements per CSP, the required transmit power per antenna scales as  $1/N^2$  and the total transmit power from a CSP scales as  $1/N$ , under ideal conditions, a property shared with massive MIMO systems [6]. If  $P$  of these CSPs are operating coherently, thus acting as one large antenna array, the corresponding scaling factors, again under ideal conditions, become  $1/(PN)^2$  per antenna and  $1/(PN)$  for the entire system. While these numbers are for idealized conditions, with perfect synchronization, even a fraction of these reductions in transmit power give a substantial decrease in the requirements per antenna/TX. This opens up for using radios with much lower power requirements.

In addition to the above array gains, a large number of antenna elements cooperating with joint processing of their signals is less susceptible to several other impairments, such as phase and quantization errors. Even systems with one-bit analog-to-digital converters (ADCs) can deliver a substantial performance [7, 8], while a few more bits in the ADCs can be more energy efficient in total [9].

While the above gives opportunities for using massive numbers of low-power/low-quality/low-cost radios for efficient communication, it is not straight-forward to find this type of hardware. Most radios today are designed for much higher performance than what is needed for each transceiver in a system with a massive number of cooperating antennas, like RadioWeaves.

In the D-MIMO/large intelligent surface (LIS) testbed built in parallel with the REINDEER project at ULUND, the LuLIS testbed, we have selected a highly linear pre-driver amplifier BTS6403U [10], from NXP, whose 29.5 dBm saturation output power is much more than what is needed. It is, however, a good idea to over-dimension testbeds, since lower performance can always be simulated in software, by limiting transmit power, discarding all but a few ADC bits, artificially introducing non-linearities, etc. Further, since the transmit power of the individual antenna elements is substantially higher than required for communication purposes, the hardware in the LuLIS testbed is quite capable of performing WPT. However, in a real deployment, the expected characteristics of the use may point towards separate radios for communication and power transfer.

### 3.2.1.2 Wireless power transfer

We here list the most important recommendations when it comes to effectively designing a CSP that support distributed radio frequency wireless power transfer in a phase coherent way, and refer to deliverable D2.3 [3] for the in-depth analysis. The hardware should be affordable and commercially attractive, meaning that e.g. direct sampling hardware is too expensive. Calculations indicate that the number of CSPs may increase rapidly to cover a massive number of energy neutral devices, while staying within the regulatory limits. In addition to the requirements to transmit signals that coherently add up on the energy neutral device (END) locations, a corresponding demodulator or phase detector is required to handle the incoming pilot messages from the ENDS. The reciprocity-based beamforming approach relies on the support of several CSP features:

- Adjustable transmit phase
- Adjustable transmit PA gain

- Provisions to perform frequency and phase calibrations
- Demodulator/phase detector for incoming signals

**Design of RF Front End** A typical software-defined radio (SDR) architecture [11] provides flexibility to generate the desired signals and demodulate incoming signals. For CSPs that support wireless power transfer only and solely act as Charging Element (CE), the IQ modulator in the transmit chain is not strictly required. This CE earlier was introduced in Figure 2.2 of D2.1.

During the REINDEER project, experiments have shown that achieving perfect phase coherence is challenging, especially with affordable SDR platforms. E.g. a B210 universal software radio peripheral (USRP) does not have an internal loop-back to synchronise the internal RF RX PLL with the internal TX PLL, meaning that an external loop-back is required. Alternatively, the leakage between RX and TX chain could be used to synchronise both PLLs. The synchronisation is required to support reciprocity based beamforming.

Moreover, a phase relation is required between multiple distributed CSPs. Since there is usually no phase relation between the 10 MHz input reference and the internal SDR PLL architectures, the designer is forced to use an external distributed phase coherent reference clock. This results in the ability to compare incoming pilot message phases with the external reference signal.

In RF transceivers, like the AD9361, several dividers are commonly located behind the PLL to improved phase noise [12]. In integer-N mode PLL, there could be a well-defined phase relation between the reference signal and the PLL output, on the condition that all dividers occur only inside the control loop. Consequently, if the internal PLLs in an SDR (based on AD9361) are set up in integer-N mode, due to the dividers, the phase error equals  $x$  time  $360/N^2$  with  $N$  the number of dividers selected by the internal PLL and  $x$  a natural number between 0 and  $N$  [13].

A better approach would consist of using other PLL architectures without dividers, meaning that a direct phase relation is available between reference signal and the output. Although the phase noise could be higher, no phase calibration procedure is required if the PLLs operate in integer-N mode. Another solution uses a similar PLL design that is set to integer-N or fractional-N mode, but with a phase synchronisation input. In this case, obtaining a highly accurate time reference, such as a pulse per second (1PPS) signal with picosecond accuracy, is essential. Achieving this level of precision presents significant challenges.

By implementing one of the proposed solutions, the phase of an incoming backscattered pilot signal can be measured reliably without the need for an additional phase calibration procedure. However, the condition remains that a highly accurate, phase-synchronous 10 MHz reference and/or phase-synchronous 1PPS signal is essential.

One of the key considerations in the CSP design is that the cost and energy consumption must be kept low. For example, the AD9363 (the lowest price category within the AD93xx series) offers a highly versatile RF front end with significant flexibility but easily costs around 120 EUR. With a bandwidth ranging from 325 MHz to 3.8 GHz, the capabilities of this RF transceiver might be over-dimensioned for a single CE within a RadioWeave infrastructure. However, this MIMO transceiver is suitable for phase-coherent operation if the designer implements and performs the calibration procedure to measure the phase relationships between the different PLLs.

In the future, it may be possible to utilize low-complexity transceiver designs, such as the *ADF7021* and *ADF7023*, having a lower price in the order of 10 EUR per IC. These predominantly narrow-band RF transceivers are adequate for operation within the ISM radio frequency identification

(RFID) frequency band. Given the relatively low data rates associated with backscatter signals, an FPGA is not strictly required and can be avoided. The demodulators within these low-complexity RF front-end designs typically include ASK and FSK demodulators, which are sufficient for demodulating backscattered signals. Again, the primary challenge remains the synchronization of the TX/RX PLL phases, both globally across the distributed architecture and locally within the RF transceiver itself.

**Power amplifier recommendations** Besides the overall CSP architecture, the required radiated power expected to be delivered by each CSP influences the power amplifier (PA) requirements. Initial calculations were performed in D2.3 [3] to estimate the individual radiated power levels. For this purpose, the most challenging electronic shelf label (ESL) use case from D1.1 was examined, and the feasibility of supporting 600 ESLs in a supermarket corridor was checked.

In this feasibility study [3], the required radiated power that each CSP must emit was investigated. It was assumed that the transmit power for each individual antenna is the same and that the radiated power remains constant over time. All available antennas were assumed to be continuously radiating. The furthest located ESL determined the radiated power for the non-coherent case. In the coherent case, the power can be adjusted according to the ESL being targeted. A further and more realistic study was later carried out and published in [14], with simulations conducted using the simulator from TU Graz (TugSim). It was found that to support 600 ESLs with 351 transmit antennas between 1 and 5 dBm for each individual patch antenna and 4 and 12 dBm for each individual dipole antenna is required in the coherent and non-coherent cases. This information can be useful for the designer of an CSP.

Using all 351 antennas in [14] to supply the ESLs with energy in a non-coherent case does not show to be the most optimal configuration of the RadioWeave infrastructure. In the non-coherent case, optimizations are feasible, with an emphasis on the number of active antennas and the corresponding transmission power. In [4], we report on an optimization related to the concept of [14] and investigated the deployment of antennas in a more optimized way. Both the engaged antennas, timeslots, and individual power per antenna are optimized by the algorithm. Instead of the supermarket corridor, the Techtile infrastructure was used to virtually power 240 ESLs.

It appears from Fig. 4 of [4] that the total transmitted power does not change in the non-coherent case. The optimization calculation shows that at a certain number of antennas, the overall efficiency will not improve anymore. In contrast to using 84 antennas like in [14], it is clear that after optimization, fewer antennas need to radiate at higher individual power levels. However, the overall efficiency will improve compared to activating all antennas at the same power level.

Furthermore, optimizations are also achievable in the coherent case. Fig. 6 of [4], for example, shows that it is more efficient to radiate at very high power levels for a short time slot. The average overall radiated power, shown in Fig. 4 [4], will be the lowest for these selection of 84 antennas and will further decrease as more antennas can be activated. The distribution of the transmit power of the 84 individual antennas in this coherent case varies between approximately 0 to 30 dBm, illustrated in Figure 3.2. Consequently, both the dynamic range and the maximum radiated power are important to realize this optimization strategy in practice.

We can conclude that the strategy and methodology proposed in [4, 14] can help the CSP designer to determine the PA requirements for the targeted use cases.

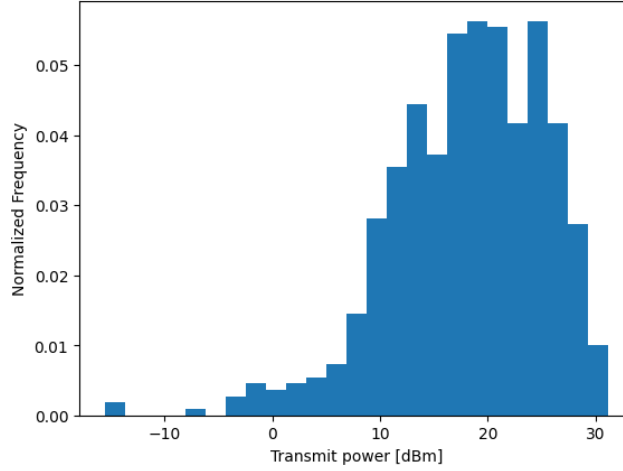


Figure 3.2: Distribution of individual radiated power levels for the 84 antennas over multiple time-slots [4].

### 3.2.2 Processing (distributed and central) and associated data exchange between nodes

We consider an uplink transmission of  $K$  single-antenna UEs in a distributed network of  $P$  CSPs, each containing  $N$  antennas. We further assume that  $NP \gg K$ . The signal received at CSP  $p \in \{1, \dots, P\}$  within a given OFDM subcarrier may be identified with an  $N \times 1$  vector of baseband symbols given by

$$\mathbf{y}_p = \mathbf{H}_p \mathbf{s} + \mathbf{n}_p, \quad (3.1)$$

where  $\mathbf{H}_p$  is the  $N \times K$  channel matrix,  $\mathbf{s}$  is the  $K \times 1$  vector of symbols transmitted by the UEs, and  $\mathbf{n}_p \sim \mathcal{CN}(\mathbf{0}, N_0 \mathbf{I}_N)$  is the AWGN vector. The network-wide received vector would then correspond to

$$\mathbf{y} = \mathbf{H} \mathbf{s} + \mathbf{n}, \quad (3.2)$$

where we have  $\mathbf{y} = [\mathbf{y}_1^T, \dots, \mathbf{y}_P^T]^T$ ,  $\mathbf{H} = [\mathbf{H}_1^T, \dots, \mathbf{H}_P^T]^T$ , and  $\mathbf{n} = [\mathbf{n}_1^T, \dots, \mathbf{n}_P^T]^T$ .

#### 3.2.2.1 Centralized Processing

In a centralized architecture, all CSPs are assumed to be connected to a central node which would have access to the whole received vector  $\mathbf{y}$ , as well as to an estimate of the whole channel  $\mathbf{H}$ . Let us assume for simplicity perfect channel estimation. Linear processing schemes could then be implemented based on  $\mathbf{H}$  to simplify the decoding of  $\mathbf{s}$  from  $\mathbf{y}$ . The most common linear processing schemes for MIMO uplink equalization are MRC, ZF, and LMMSE [15], whose equalization matrices may be respectively given by

$$\mathbf{W}_{\text{MRC}} = \mathbf{H}^H, \quad (3.3a)$$

$$\mathbf{W}_{\text{ZF}} = (\mathbf{H}^H \mathbf{H})^{-1} \mathbf{H}^H, \quad (3.3b)$$

$$\mathbf{W}_{\text{MMSE}} = (\mathbf{H}^H \mathbf{H} + N_0 \mathbf{I}_K)^{-1} \mathbf{H}^H. \quad (3.3c)$$

The  $K$  entries of the post-processed vector  $\mathbf{z} = \mathbf{W} \mathbf{y}$  may then be used to independently decode the information transmitted by each UE.



### 3.2.2.2 Decentralized Processing

In a decentralized architecture, the assumption of having  $\mathbf{y}$  and  $\mathbf{H}$  available at a central node becomes unreasonable. Instead, if each CSP is assumed to have channel estimation capabilities, CSP  $p$  may only have direct access to its received vector  $\mathbf{y}_p$ , as well as to the estimate of its respective local channel  $\mathbf{H}_p$ . Implementing linear processing schemes as those in (3.3) becomes a challenging task strongly dependent on the topology and interconnection limitations of the network. Next, we provide some key observations that may be useful in defining processing strategies for a decentralized architecture [16].

**Observation 1.** *The post-processed vector after MRC processing may be expressed as a sum of local-MRC post-processed vectors by*

$$\mathbf{z}_{\text{MRC}} = \sum_{p=1}^P \mathbf{H}_p^H \mathbf{y}_p. \quad (3.4)$$

**Observation 2.** *The post-processed vector after ZF and LMMSE processing may be respectively expressed in terms of the channel Gram matrix  $\mathbf{G} = \mathbf{H}^H \mathbf{H}$ , as well as the MRC post-processed vector in (3.4), by*

$$\mathbf{z}_{\text{ZF}} = \mathbf{G}^{-1} \mathbf{z}_{\text{MRC}}, \quad (3.5)$$

$$\mathbf{z}_{\text{LMMSE}} = (\mathbf{G} + N_0 \mathbf{I}_K)^{-1} \mathbf{z}_{\text{MRC}}. \quad (3.6)$$

**Observation 3.** *The channel Gram matrix may be expressed as a sum of local channel Gram matrices by*

$$\mathbf{G} = \sum_{p=1}^P \mathbf{G}_p, \quad (3.7)$$

where  $\mathbf{G}_p = \mathbf{H}_p^H \mathbf{H}_p$  is the local channel Gram matrix for CSP  $p$ .

From the previous observations, we may note that the common MIMO equalization schemes given in (3.3) may be implemented in a decentralized architecture as long as we are able to accumulate and share the local channel Gram matrices and local-MRC post-processed vectors throughout the network. Again, how this is done depends on the specific topology and interconnection limitations, which will be discussed next.

An important goal of decentralized processing in large-scale multi-antenna systems is to limit the interconnection bandwidth so that the whole network becomes scalable as the number of CSPs and/or CSP antennas grow. However, if we want the network to serve several users transmitting simultaneously, it is inevitable that the required resources scale with the number of simultaneous users, otherwise some of the end data from the users should be dropped. Hence, we focus on studying decentralized solutions where the interconnection bandwidth can scale with the number of users  $K$ , but not with the total number of antennas  $M \triangleq NP$  as happens with centralized solutions. Moreover, we are especially interested in solutions that allow us to achieve the equalizers from (3.3) without any performance loss compared to if they were implemented in a centralized architecture. We thus proceed to discuss how to achieve the mentioned equalizers, and what are the associated trade-offs when considering several common interconnection topologies depicted in Figs. 3.3-3.6, where each node corresponds to a CPS and each directed edge corresponds to a data link. In all cases, each CSP is assumed to have baseband processing capabilities, including channel estimation.

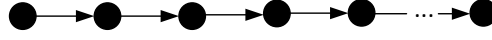


Figure 3.3: Daisy chain topology.

### 3.2.2.3 Daisy chain topology

The Daisy chain, illustrated in Fig. 3.3, corresponds to the simplest of all decentralized topologies. In this case, the CSPs are sequentially connected through unidirectional links. The number of unidirectional links is thus given directly by

$$L_{u,D-Ch} = P - 1. \quad (3.8)$$

Considering Observation 1, we can achieve MRC equalization by simply performing local-MRC at each CSP, and aggregating the respective post-processed vectors throughout the Daisy chain. Thus, assuming the CSPs indexes are ordered according to the position in the chain, CSP  $p$  would have obtained its  $K \times 1$  local post-processed vector

$$\mathbf{z}_{\text{MRC},p} = \mathbf{H}_p^H \mathbf{y}_p, \quad (3.9)$$

which would be added to the  $K \times 1$  aggregated MRC-post-processed vector received from CSP  $p - 1$

$$\begin{aligned} \mathbf{z}_{\text{MRC},(p-1 \rightarrow p)} &= \sum_{i=1}^{p-1} \mathbf{z}_{\text{MRC},i} \\ &= \sum_{i=1}^{p-1} \mathbf{H}_i \mathbf{y}_i. \end{aligned} \quad (3.10)$$

The resulting  $\mathbf{z}_{\text{MRC},(p \rightarrow p+1)} = \mathbf{z}_{\text{MRC},(p-1 \rightarrow p)} + \mathbf{z}_{\text{MRC},p}$ , would then be forwarded to CSP  $p + 1$ . Once the final CSP  $P$  has received the aggregated post-processed vector  $\mathbf{z}_{(P-1,P)}$  and added its local post-processed vector  $\mathbf{z}_P$  the result would trivially correspond to the MRC post-processed vector  $\mathbf{z}_{\text{MRC}}$  from (3.4).

Considering Observation 2, in order to perform ZF or MMSE it is enough to have at one of the nodes access to both the MRC post-processed vector,  $\mathbf{z}_{\text{MRC}}$ , as well as the complete channel gram matrix,  $\mathbf{G}$ . We have previously explained how to obtain  $\mathbf{z}_{\text{MRC}}$  at the final node of the chain by sequentially accumulating the local-MRC post-processed vectors,  $\mathbf{z}_{\text{MRC},p}$ , throughout the Daisy chain. Considering Observation 3, we can also compute the local Gram matrices,  $\mathbf{G}_p$ , at each CSP, and accumulate them throughout the chain. In this case, in addition to the  $K \times 1$  aggregated MRC-post-processed vector  $\mathbf{z}_{\text{MRC},(p-1 \rightarrow p)}$ , each unidirectional link,  $(p - 1, p)$  for  $p \in \{2, \dots, P\}$ , would need to share a  $K \times K$  matrix associated to the aggregated Gram matrices

$$\begin{aligned} \mathbf{G}_{(p-1 \rightarrow p)} &= \sum_{i=1}^{p-1} \mathbf{G}_i \\ &= \sum_{i=1}^{p-1} \mathbf{H}_i \mathbf{y}_i. \end{aligned} \quad (3.11)$$

Note that the computation and sharing of  $\mathbf{G}_{(p \rightarrow p+1)}$  and  $\mathbf{z}_{(p \rightarrow p+1)}$  at CSP  $p$  may be done parallelly since these do not depend upon each other.

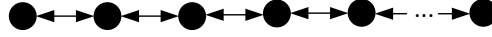


Figure 3.4: Bidirectional chain topology.

From the previous decentralized sharing schemes, each unidirectional link in Fig. 3.3 would only have to support the transmission of a  $K \times 1$  vector, for the MRC case, or a  $K \times 1$  vector plus a  $K \times K$  Hermitian matrix—i.e., containing only  $K(K + 1)/2$  distinct numbers—for the ZF/LMMSE case. Thus, the data being shared does not scale with the number of CSPs or CSP antennas, but only with the number of users as intended. However, the delay to perform such processing would scale linearly with the number of jumps that the data has to take before it arrives to the last CSP. We may easily notice that said number of jumps is given by

$$J_{\text{D-Ch}} = P - 1 \quad (3.12)$$

so that the corresponding delay has linear scaling  $J_{\text{D-Ch}} \sim P$  for large  $P$ .

### 3.2.2.4 Bidirectional chain topology

A direct extension of the Daisy chain topology from Fig. 3.3 is to consider a chain topology, but where the links are bidirectional instead of unidirectional. We term this type of topology *bidirectional chain topology*, which is depicted in Fig. 3.4, and where the number of bidirectional links is

$$L_{\text{b,B-Ch}} = P - 1. \quad (3.13)$$

Note that number of bidirectional links in (3.14) is equal to the number of unidirectional links in (3.8), but a bidirectional link may be seen as two unidirectional links since it requires twice the resources to support a bidirectional communication link with the same characteristics. Thus, to facilitate comparison we may compute the number of unidirectional links in this topology as

$$L_{\text{u,B-Ch}} = 2(P - 1). \quad (3.14)$$

As happened in the Daisy chain topology, we can also perform MRC and ZF/MMSE by simply sharing and accumulating at each CSP the local-MRC processed vectors  $z_{\text{MRC},p}$  and the local channel Gram matrices  $G_p$ . However, in order to avoid repeated sum elements in the aggregated data we have the extra requirement that the CSPs should distinguish the two possible directions of the aggregated data. Hence, this may be seen as two Daisy chain topologies sharing non-interfering data in both directions.

One benefit of the bidirectional chain topology is that all CSPs could eventually (after  $P - 1$  jumps) have access to  $z_{\text{MRC}}$  (and  $G$ ), so that any of them would be able to perform decoding. This gives more flexibility in the exploitation of the network. Moreover, the minimum number of jumps that the data has to travel for achieving without loss the MIMO linear equalizers from (3.3) is now reduced to

$$J_{\text{B-Ch}} = \lfloor P/2 \rfloor, \quad (3.15)$$

which corresponds to the number of jumps required for the central node to have the whole  $z_{\text{MRC}}$  (and  $G$ ). This corresponds to a scaling of  $J_{\text{B-Ch}} \sim P/2$  for large  $P$ .

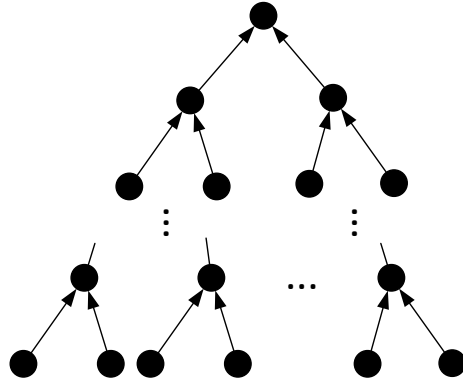


Figure 3.5: Binary tree topology.

### 3.2.2.5 $Q$ -ary tree topology

This topology corresponds to an alternative extension of the Daisy chain topology where the nodes are distributed into layers such that each node is connected to  $Q$  nodes from the subsequent layer via unidirectional links. For a fixed total number of nodes  $P$ , the required number of layers corresponds to

$$N_{\text{layers}} = \lceil \log_Q(PQ - P + 1) \rceil. \quad (3.16)$$

Fig. 3.5 depicts a binary tree topology to give a simple example of a  $Q$ -ary tree topology for  $Q = 2$ .<sup>1</sup> It is important to note that the unidirectional links should go from lower layers (i.e., having more nodes) to upper layers (i.e., having less nodes) to allow for sharing schemes with minimum number of jumps. The number of unidirectional links in this topology is then given by

$$L_{\text{u},Q\text{-tree}} = P - 1, \quad (3.17)$$

since each node is connected to a single layer from the upper layer except for the top layer node.

In order to share the necessary data to be able to implement the MIMO linear processing schemes from (3.3), we can note that each node from the bottom layer of the  $Q$ -ary tree forms a  $\log_Q(P+1)$ -sized Daisy chain towards the origin node at the top of the  $Q$ -ary tree. Thus, for each of these chains we can share and aggregate the local MRC-post-processed vectors (and local Gram matrices) in the same way as in the Daisy chain. Moreover, each node can aggregate the incoming contributions from the  $Q$  connected nodes in the layer below to maintain the scaling of the data shared through each link, while allowing for parallel sharing of the contribution from each layer. With the previous considerations, the total number of jumps would be given by

$$\begin{aligned} J_{Q\text{-tree}} &= N_{\text{layers}} - 1 \\ &= \lceil \log_Q(PQ - P + 1) \rceil - 1 \end{aligned} \quad (3.18)$$

which, for large  $P$ , scales as  $J_{Q\text{-tree}} \sim \log_Q(P)$ —as seen from (3.16).

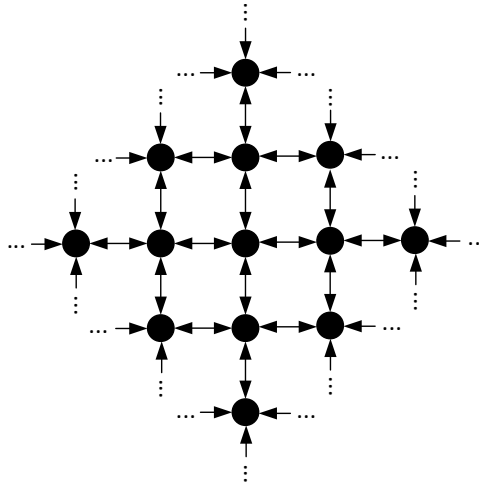


Figure 3.6: Square grid topology.

### 3.2.2.6 Square grid topology

In some scenarios it may be desirable to deploy CSPs following a grid pattern, e.g., when covering a wall/ceiling with CSPs consisting of square antenna arrays. In such cases, it would be interesting to consider an alternative topology where each CSP is connected to its 4 neighboring CSPs within the grid. Moreover, to have full flexibility we may assume that the links between CSPs are bidirectional. These considerations lead to the what we term the *square grid topology*, depicted in Fig. 3.6.

Sharing and aggregating the local-MRC processed vectors  $z_{\text{MRC},p}$  (and the local channel Gram matrices  $G_p$ ) in the square grid topology becomes specially challenging. The reason is the potential presence of loops in the paths followed by the aggregated data, which may lead to some contributions being added several times. Thus, as happened with the bidirectional-chain topology, the square grid topology requires the nodes to distinguish the direction of flow of the aggregated data. If there is no orchestration between nodes, we may assume that each node aggregates its inputs with its own contribution and shares the results to its neighbors after every iteration. However, to avoid back-propagating a contribution, each node would only allow transmitting the aggregated data received from one neighboring node (after adding its own contribution) towards neighboring nodes different from the one where it was originated. Moreover, to avoid loops after several iterations, each node would aggregate all 3 inputs with its own contribution throughout one of the axis (e.g., horizontal), while throughout the other axis (e.g., vertical) it would only aggregate one input with its own contribution and redirect it to the opposite direction. This scheme is analogous to the 2D sharing scheme proposed in [17], which is there used to share AND aggregate without loops the residual interference within one panel of antennas. Fig. 3.7 illustrates how each node aggregates and shares data within the proposed scheme. Note that all nodes should only need distinguish the global vertical and horizontal axes of the grid topology they are connected to, but the scheme would still work if the vertical and horizontal axes are interchanged for all nodes.

<sup>1</sup>Note that for  $Q = 1$  the topology degenerates to the Daisy chain depicted in Fig. 3.3.

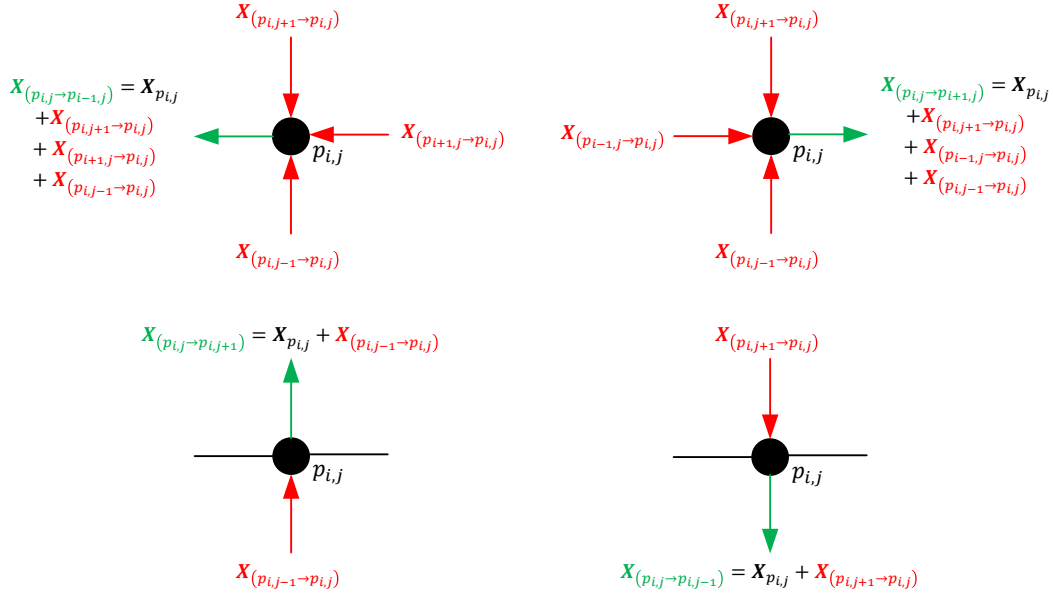


Figure 3.7: Node aggregation for square grid topology, where  $\mathbf{X} \in \{z_{\text{MRC}}, \mathbf{G}\}$  corresponds to the data to be aggregated.

Similar to the  $Q$ -ary tree topology, we can also divide the square grid topology into a number of layers starting from the most inner (centric) node towards the outer nodes. Assuming that the  $P$  nodes are uniformly arranged keeping the same form factor as Fig. 3.6 (except for possible cropping in the outer most layer), the total number of layers would then be given by

$$N_{\text{layers}} = \left\lceil \frac{\sqrt{2P-1} + 1}{2} \right\rceil. \quad (3.19)$$

Let us assume that  $P$  is chosen so that the outer most layer is complete, i.e., there is no need to consider the ceil operator in (3.19). The total number of bidirectional links would be given by

$$\begin{aligned} L_{\text{b,sq-grid}} &= \sum_{i=1}^{N_{\text{layers}}-1} 4(2i-1) \\ &= 4(N_{\text{layers}}-1)^2 \\ &= 2P - 2\sqrt{2P-1}, \end{aligned} \quad (3.20)$$

which scales as  $2P$  for large  $P$ . Again, we could translate each bidirectional link to two unidirectional links leading, which would double the respective scaling. Each unidirectional link would still have to transmit data which scales with the number of users  $K$  either linearly (for MRC) or quadratically (for ZF or MMSE). On the other hand, the minimum number of jumps required until one CSP (i.e., the most centric one) would have access to the complete  $z_{\text{MRC}}$  (or  $\mathbf{G}$ ) is given by

$$\begin{aligned} J_{\text{b,sq-grid}} &= N_{\text{layers}} - 1 \\ &= N_{\text{layers}} - 1 \\ &= \frac{\sqrt{2P-1} - 1}{2}, \end{aligned} \quad (3.21)$$

which scales as  $J_{b,\text{sq-grid}} \sim \sqrt{2P}$  for large  $P$ .

### 3.2.3 Calibration and synchronization

As pointed out by REINDEER partners in [18]<sup>2</sup>, when discussing 6G testbeds, a main challenge in most wireless systems is *calibration* and *synchronization*. We use the word calibration in a general sense, including gain and phase calibration, linearization, in-phase and quadrature (IQ) imbalance compensation, and impairment mitigation in general. Synchronization includes mismatch and drift related to the oscillators, e.g., phase, sampling time, and carrier frequency calibration. Many of the characteristics of testbeds for evaluating RadioWeaves carries over correspondingly to a RadioWeaves deployment. Let us have a closer look at calibration and synchronization.

**Calibration** To calibrate a transmitter, it is necessary to capture the transmitted signal to enable later characterization and compensation, which is historically often achieved by observation receivers at the transmitter outputs. However, in a multi-antenna transmitter, the overall transmitted signal is a combination of all the antenna signals, and the output of individual transmitters is not representative of what the receivers will see. Further, with the development towards integrated systems, accessing the signals at the transmitter outputs can be difficult. These challenges require OTA signal acquisition for calibration, generally through one or more external receivers.

With phased-array beamforming (BF), needing knowledge of beam directions, absolute calibration is required, i.e., the transmitters and receivers are each calibrated to reach the desired linear operation as accurately as possible [19]. In contrast, for reciprocity-based communication, as in massive MIMO (mMIMO), it is enough to ensure that TX and receiver (RX) RF chains are reciprocal [20] using *reciprocity calibration*. This calibration can be done in collaboration with the user equipments (UEs) by pilot signalling [20], but it is preferable to avoid this. In [21] and [22] the authors have proposed to instead exchange pilots only between the CSPs, possibly using an additional external reference antenna. Alternatively, In [23] the authors show that pilot-free calibration can be performed by exploiting antenna coupling. OTA linearization (i.e., compensation of nonlinear amplifiers) in a multiple-input multiple-output (MIMO) setting is studied in, e.g., [24]. The calibration challenge in D-MIMO is similar to the challenge in co-located MIMO. However, the issue of synchronization is more challenging for distributed systems; we discuss this below.

**Synchronization** Synchronization, i.e., calibration connected to oscillators, is a crucial topic in communication networks. Tab. 3.1 summarizes methods for synchronization and indicates whether they are suited for co-located or distributed systems, as well as applicable to sub-10 GHz or millimeter wave (mmWave) carrier frequencies. Overviews of timing and carrier synchronization algorithms, for co-located and distributed MIMO systems, can be found in [25] and [26]. In a multi-user MIMO system, the UEs have their own independent oscillator, which poses multiple synchronization tasks for each CSP. With co-located MIMO, the oscillators or PLLs can be shared among the antennas. However, in a D-MIMO system, this mechanism does not scale well with increased geographical distance between the CSPs. The synchronization is one of the critical issues in D-MIMO, and it is therefore of high priority to study in 6G testbeds in general, and for RadioWeaves in particular.

Beamforming relies on multiple antennas, operating in a phase-synchronous way, such that the receivers experience constructive addition of multiple antenna signals. To achieve such phase-

<sup>2</sup>Contributions by Thomas Eriksson and Christian Fager in the 6GTandem project are greatly appreciated.

Table 3.1: Calibration and Synchronization mechanisms employed in 6G testbeds. Addressing the calibration issue is indicated by ✓. How well the mechanism can scale with both the geographical dispersion and the number of CSPs in D-MIMO is marked by, ●○○, ●●○ and ●●●. More details regarding the mechanisms can be found in the included references (Ref. column).

Mechanism	Frequency		Phase Offset	Time Offset	D-MIMO	Carrier		Ref.
	Drift	Offset				Sub-10GHz	mmWave	
RF and BB PLL sharing	✓	✓	✓	✓		✓		
Reference clock (e.g., 10 MHz and 1PPS)	✓	✓		✓	●○○	✓	✓	[27, 28, 28, 29]
Ethernet-based								
White Rabbit	✓	✓	✓	✓	●●●	✓	✓	[29, 30]
Precision-time protocol (PTP)	✓	✓		✓	●●●	✓	✓	[27, 31, 32]
Over-the-air								
UE-assisted sync	✓	✓	✓	✓	●●●	✓	✓	[22, 33]
Beacon/anchor nodes	✓	✓	✓	✓	●●○	✓	✓	[34, 35]
Radio-over-fiber								
Analog	✓	✓	✓	✓	●●○	✓	✓	[36, 37]
Digital ( $\Sigma\Delta$ )	✓	✓	✓	✓	●●○	✓	✓	[38–40]

coherent downlink (DL) transmission, or uplink (UL) reception, carrier frequency, sample time and phase must be accurately synchronized. When the signals are not phase-aligned at the user, they no longer constructively interfere, degrading the signal power and quality. The techniques to obtain coherency can be divided into connected synchronization, i.e., using cables or optical fibers, or wireless OTA synchronization. Connected synchronization can be performed by sharing the RF oscillator between the radios. As mentioned, this is problematic for high frequencies and when the distances to remote antennas increases. An alternative is to share a low-frequency reference clock (e.g., at around 10 MHz), which can be combined with a 1PPS signal. This approach is also used in the Techtile testbed in REINDEER. To improve the scalability further, Ethernet-based approaches can be implemented, such as White Rabbit (WR) [41]. This is illustrated in Figure 3.8a. To achieve a synchronized and phase coherent MIMO DL, an all-digital radio-over-fiber (RoF) solution using bandpass  $\Sigma\Delta$  coding has been proposed [38], depicted in Figure 3.8b. Compared to analog RoF solutions, it enables a relatively simple and low-cost and low-complex implementation CSPs [39, 40, 42]. There are also several OTA techniques proposed in the literature. Carrier frequency, sample time and phase can be estimated and compensated, using pilots shared with the UEs [22] or feedback signalling [33, 43]. Some proposals in the literature assume a beacon signal transmitted by a central node [34], potentially leading to problems when the number of CSPs are scaled up. Decentralized schemes, e.g., based on multiple anchor nodes, are studied in, e.g., [31, 35]. The most suitable solution for a RadioWeaves implementation will depend on the characteristics of the deployment. This is a complicated design choice that still needs to undergo realistic testing. With more, and increasingly sophisticated, testbeds becoming available, we foresee important advances in the next few years.



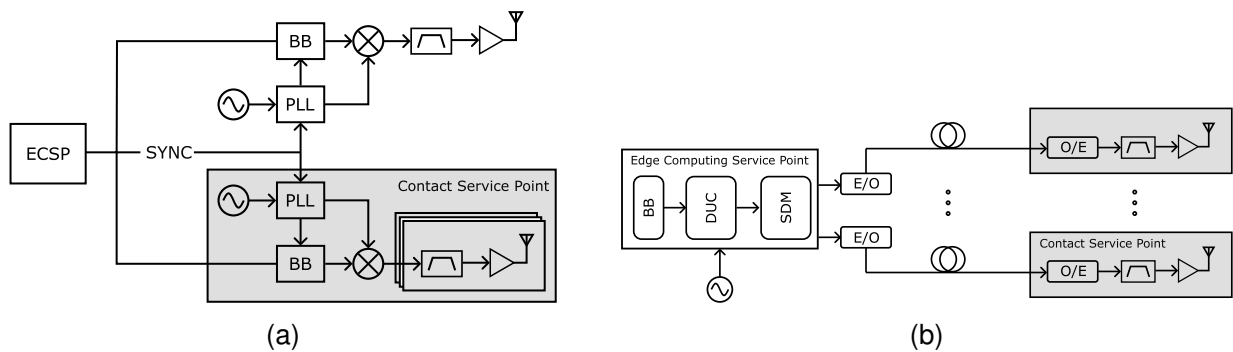


Figure 3.8: Synchronization mechanisms between distributed CSPs using (a) a sync signal and (b) SDoF. The sync signal can be either an Ethernet-based or dedicated cabling or OTA technique, the principle remains that instead of sharing a LO, the PLL is calibrated based on an external sync signal. Used abbreviations: base-band (BB), digital up-converter (DUC), sigma-delta modulator (SDM), optic-to-electrical (O/E).

# Chapter 4

## Energy efficiency analysis

### 4.1 Energy efficiency overview

Minimizing energy consumption in any system is trivial: Just turn it off. Instead, energy consumption should always be minimized with the constraint that a given set of performance requirements (e.g., user throughput, capacity, latency, etc.) is still fulfilled. Sometimes this type of energy consumption minimization with performance requirement constraints is denoted *Energy Performance*.

Several things impact the energy consumption of a telecommunication system: the standard, the requirements, the hardware and software implementation, and the traffic are all major factors. And for a system to be energy efficient, all parts of the system have to be energy efficient. For example, having a standard that enables very energy efficient implementation and deployment is not sufficient. The implementation also needs to utilize the energy saving potential that the standard enables. Often it only takes one mistake, one bad shortcut, to destroy the energy efficiency of an otherwise excellent system.

Minimizing energy consumption (for a set of performance requirements) is important from at least three different perspectives: engineering, economy and ecology.

One engineering-related aspect is that energy consumption generates heat, which needs to be handled. And thermal management solutions increase size, weight, and cost of the product. For RadioWeaves, miniaturization of distributed hardware components is key for success and the form factors required will not be possible without very low energy consumption.

In terms of economy, electricity cost can become substantial unless the system is energy efficient. It is particularly important from an economical perspective that the energy consumption when there is zero traffic is sufficiently low. No operator wants to pay more for the electricity cost than what they earn from serving user traffic. A system with a high fixed energy cost can only be accepted in small areas where the total energy cost adds up to an acceptable small number despite the inefficiencies. But if we want RadioWeaves to be a scalable solution with a large footprint in future networks, then low operational cost through low energy consumption is a must.

The ecological perspective involves both embedded and operational impacts. The embedded impact is partly minimized by miniaturization of products, which requires low energy consumption, as mentioned above. It is also partly minimized by high performance (which is included in the Energy Performance metric) such that less infrastructure hardware is required. The operation

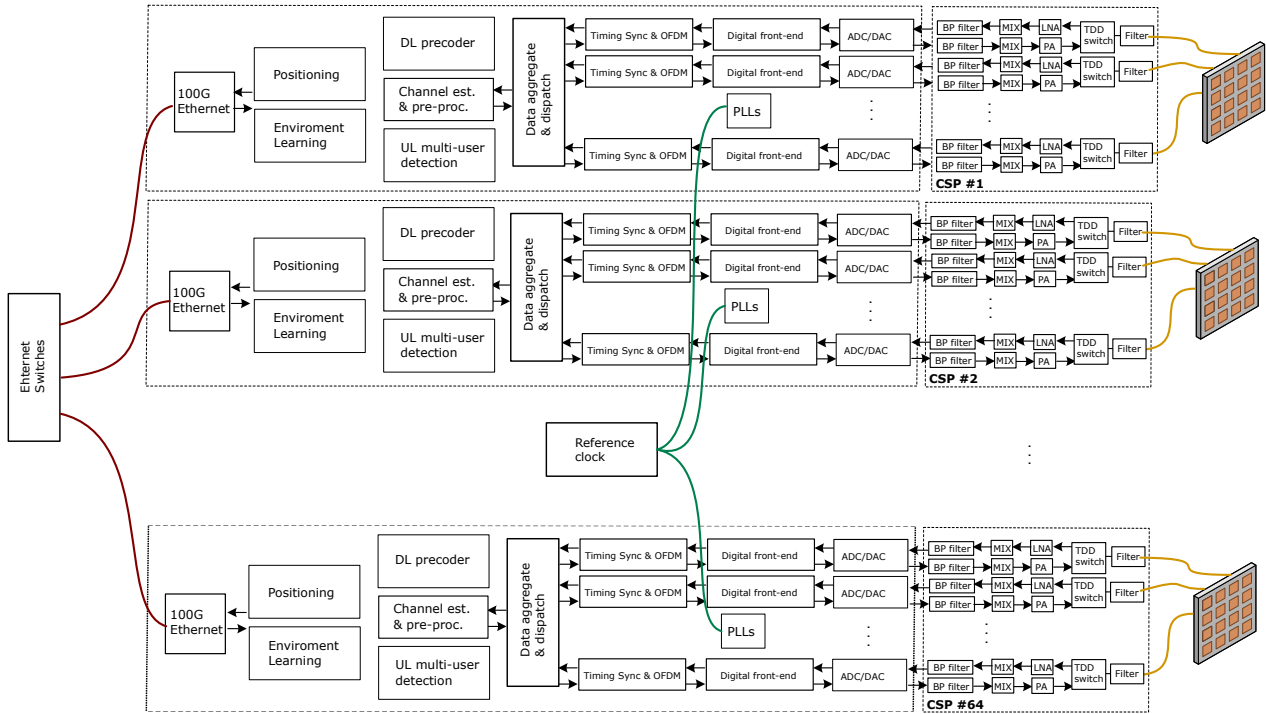


Figure 4.1: High-level block diagram of the RadioWeaves hardware.

energy is reduced by consuming as little energy as possible both when serving users with data, and when not serving users with data. An operator who wants to reduce the climate impact of its operation has two options: Either reduce the operational energy consumption of the network, or ensure that the network operates on clean energy.

## 4.2 Energy consumption models

Fig. 4.1 shows the high-level overview of (both analog and digital) processing components and blocks in a typical RadioWeaves system. Table 4.1 lists the corresponding power/energy consumption model of different hardware components in the systems, including analog processing, digital processing, memory systems, interconnections, and synchronization systems. The power consumption model is a mixture of configurable design parameters and results extracted from implementation examples.

The choice of design parameters depends on many aspects. For instance, the PA output power, the resolution and sampling rate of data converters depend on the system setup (e.g., number of antennas, system bandwidth), the use cases (e.g., number of users, the required quality of service), and the channel environments. The general trend is that we can use less powerful PA and lower resolution data converters when increasing the number of antennas.

The power of computation and memory access highly depend on the processing algorithm selected, the architecture (e.g., topology) of the RadioWeaves, as well as the frame structure. The power consumption of data transfer between different hardware units inside RadioWeaves can be significant, especially when the units are distributed over long distance. The data rate on the interconnections will be decided by the RadioWeaves architecture and how the processing is distributed. The synchronization system power consumption will depend on the frequency band

Table 4.1: Hardware components in RadioWeaves and power/energy consumption model

<b>Analog Processing</b>	
Power amplifier	$(P_{in} + P_{out}/\eta) \times \# \text{ transmitters}^a$ [44]
ADC	$(\alpha 2^b f W) \times \# \text{ digital path}^b$ [45]
DAC	$(\beta 2^b f W) \times \# \text{ digital path}^c$
<b>Digital computation and storage</b>	
Operation (multiplier/MAC)	$3.1 \text{ pJ} \times \# \text{ operation per second (32bit Mult, 45nm)}$ [46]
On-chip SRAM Memory access	$5 \text{ pJ} \times \# \text{ SRAM access per second (32bit for 32KB SRAM)}$ [46]
Off-chip DRAM Memory access	$640 \text{ pJ} \times \# \text{ DRAM access per second (32bit)}$ [46]
<b>Data transfer and interconnection</b>	
Local links	$5.34 \text{ pJ/bit} \times \# \text{ bps (SerDes, 65nm)}$ [47]
Back-plane	$45 \text{ pJ/bit} \times \# \text{ bps (100G Ethernet, 65nm, PHY only, no switch/router)}^d$ [48]
	$5.2 \text{ nJ/bit} \times \# \text{ bps (100G Ethernet, Switch)}$ [49]
<b>Synchronization</b>	
Clock distribution	$2.2 \text{ W} \times \# \text{ white rabbit nodes}$ [50] (Can be partially merged with back-plane)

<sup>a</sup>  $P_{in}$  is the PA input power,  $P_{out}$  is the PA output power,  $\eta$  is the PA efficiency, e.g., 0.15-0.25 for class AB

<sup>b</sup>  $\alpha$  is ADC FoM factor (fJ/conv-step), e.g., 165 for 28nm 10bit, 5GS/s ADC; 44 for 28nm 600MS/s, 12bit ADC,  $b$  is effective bit resolution,  $f$  is conversion rate

<sup>c</sup>  $\beta$  is DAC FoM factor,  $b$  is effective bit resolution,  $f$  is conversion rate

<sup>d</sup> Similar results in the power consumption (1-3W) of QSFP module for 100G Ethernet

the system is operating, the geometrical distribution of RadioWeaves, and also the system-level requirement on synchronization.

## 4.2.1 Analog blocks

In this section, we summarize the energy model of the analog RF front-end. Suppose that the transceiver has three modes of operation: active, sleep and transient. Additionally, we assume that  $L$  bits are transferred during a period of

$$T = T_{on} + T_{sp} + T_{tr} \quad (4.1)$$

where  $T_{tr}$  is the transient time from sleep to active and the transient time from active to sleep can be neglected. Hence, the total energy consumption per bit is:

$$E_b = (P_{on} \cdot T_{on} + P_{sp} \cdot T_{sp} + P_{tr} \cdot T_{tr}) / L \quad (4.2)$$

The start-up process time of each module can also be neglected in comparison with the frequency synthesizer, so

$$T_{tr} \approx T_{syn} \quad (4.3)$$

As the frequency synthesizer is found in the transmitter and the receiver (See Figure 4.1), the transient mode power consumption is commonly assumed as

$$P_{tr} \approx 2 \cdot P_{syn} \quad (4.4)$$

The active mode power consumption  $P_{on}$  can be described as the sum of circuit power  $P_c$ , transmission power  $P_t$ , and power amplifier (PA) power  $P_{PA}$ .

$$P_{on} = P_c + P_t + P_{PA} \quad (4.5)$$

According to Figure 4.1, we can write

$$P_c = P_{LNA} + 2 \cdot P_{Mixer} + P_{IF,Rx} + P_{IF,Tx} + 2 \cdot P_{syn} \quad (4.6)$$

The PA power consumption is proportional to the transmit power

$$P_{\text{PA}} = \alpha \cdot P_{\text{t}} \quad (4.7)$$

with  $\alpha = \frac{1}{\eta} - 1$ , where  $\eta$  is the drain efficiency of the PA defined as

$$\eta = \frac{P_{\text{t}}}{P_{\text{t}} + P_{\text{PA}}} \quad (4.8)$$

We also have

$$P_{\text{t}} = P_{\text{r}} \cdot G_{\text{d}} \quad (4.9)$$

where

$$G_{\text{d}} = \frac{(4\pi \cdot d_{\text{sd}})^2}{G_{\text{r}} \cdot G_{\text{t}} \cdot \lambda^2} \quad (4.10)$$

is the power gain factor, assuming a distance  $d_{\text{sd}}$  between the transmitter and the receiver, and corresponding antenna gains and wavelength. The received power can be expressed as

$$P_{\text{r}} = \gamma \cdot B \cdot N_0 \cdot N_{\text{f}} \quad (4.11)$$

where  $N_0$  is the PSD of the channel noise,  $N_{\text{f}}$  is the Noise Figure (NF) of the receiver, and  $\gamma = \frac{E_{\text{s}}}{N_0}$  is the SNR of the channel with  $E_{\text{s}}$  being the symbol energy. The drain efficiency of the PA in its simplest form can be approximated as

$$\eta = \eta_{\text{max}} \left( \frac{P_{\text{t}}}{P_{\text{t,max}}} \right)^{\beta} \quad (4.12)$$

The parameter  $\beta$  can be fit to the selected PA. A typical value would be between 0.4 and 0.5.

## 4.2.2 Digital signal processing

The power consumption of digital signal processing depends on many aspects, including the hardware architecture (ASIC, ASIP, FPGA, GPU), the semiconductor technology node, and the how the algorithms are mapped to the hardware, especially the data flow. To facilitate this high-level power consumption analysis, we apply the following (simplified) model based on the number of arithmetic operations needed per second to finish a specific digital signal processing task, e.g., operations per second (OPs/s), e.g.,

$$P_{\text{dsp}} = E_{\text{op}} \times \# \text{ operation per second} \quad (4.13)$$

Here we use a two-input multiplier as the typical arithmetical operation. Every arithmetic operation implies operands fetching from and result writing to storage element like register files, on-chip SRAM, or off-chip DRAM. Thereby,

$$E_{\text{op}} = E_{\text{mac}} + 3E_{\text{reg}} + \alpha E_{\text{sram}} + \beta E_{\text{dram}} \quad (4.14)$$

It is very difficult to have precise numbers for  $\alpha$  and  $\beta$ , which depends on the memory hierarchy, algorithm mapping, processing architecture, etc. The analysis of mapping the Gram matrix calculation,  $\mathbf{H}^H \mathbf{H}$ , (the dimension of  $\mathbf{H}$  is  $128 \times 16$ ) on a  $16 \times 16$  systolic array [51] accelerator shows around 10% for  $\alpha$  and 0.5-1% for  $\beta$ . However, if we go for more general-purpose processor architecture,  $\alpha$  and  $\beta$  will increase significantly. For instance, mapping the same Gram

matrix calculation on a 16-lane vector processing core (with limited number of vector registers) can result in  $\alpha$  closer to 100%.

Potential overhead in instruction (fetching and decoding) and controlling should be considered. The power on the clock network is also non-negligible. Based on our experience and using ASIP (e.g., with application-specific complex instructions) as an example platform, the instruction/control add another 15-20% power overhead. A simplified semiconductor technology node scaling can be done as

$$s_{\text{technode}} = \frac{\text{node}_1}{\text{node}_2} \times \left( \frac{V_1}{V_2} \right)^2. \quad (4.15)$$

For example, changing the semiconductor technology node from 40nm with a supply voltage of 0.9v to 22nm with a supply voltage of 0.8v can scale down the energy consumption by factor of around 2.3 according to (4.15).

### 4.2.3 Data shuffling

The corresponding energy for data shuffling among CSPs, e.g., pJ/bit, depends on the interconnection technology used. For simplicity, we use SerDes for local links which connect CSP processing chips on board level. For CSPs that are apart with some distance, high-speed Ethernet is used in the energy model. Depending on the number of CSPs connected, one may need high-speed Ethernet switches which is of power hungry.

## 4.3 RadioWeaves case studies

### 4.3.1 Optimizing downlink communication considering the total energy consumption

*The following is adopted from [52]. This work includes partners not involved in the REINDEER project. The co-authors have confirmed that the material could be included in this deliverable. An extension of this work is adopted and discussed in [53].*

The hardware model used in this work is adopted from Section 4.2. An overview of the hardware blocks and their energy expenditure in this work is summarized in Table 4.2 and Table 4.3. The CSPs are coordinated by one or more edge computing service points (ECSPs). In this work, the model assumes that the ECSPs are only responsible for the data transfer and thus only the energy consumption of data aggregation is included.

**Fronthaul** In this system, an Ethernet-based fronthaul is assumed, where synchronization, data, and control are multiplexed over the same cables. In this network, all CSPs and ECSPs have a WR core [60] providing time, phase, and frequency synchronization. WR is a system using well-established IEEE Ethernet-based standards, i.e., timing protocols (Synchronous Ethernet (SyncE) and PTP) to distribute time over a network. In addition, it uses phase frequency detectors to measure the fine-grained phase difference between all nodes in the network [60], thereby attaining picosecond-level synchronization. For this reason, White Rabbit is being actively studied to enable practicable and scalable cell-free massive MIMO (CF-mMIMO) systems [41, 61].

The energy consumption of the ECSPs is entirely defined by this fronthaul, i.e., the Ethernet link and one WR core.

Table 4.2: Considered energy consumption model and parameters of the system (Part 1).

	Symbol	Expression	Unit	Ref.
<b>Component</b>				
Power amplifier	$P_{PA}$	$1/\eta_{\max} \sqrt{P_{t,\max}} \sqrt{P_t}$	W	[54]
DAC/ADC	$P_{DAC}$	$FoM_W 2^b f_s$	W	[55]
White Rabbit core	$P_{sync}$	2.2	W	[56]
Ethernet link	$P_{eth}$	$7^\ddagger$	W	[57]
<b>Process</b>				
DSP operation	$E_{op}$	$\zeta(E_{mac} + \alpha E_{sram} + \gamma E_{dram})$	J/oper	
Channel estimation	$E_{CE}$	$2MK E_{op} \tau_p$	J	[55]
Linear processing	$E_{LP}$	$2MK E_{op} (\tau_c - \tau_p)$	J	[55]

$^\ddagger$  based on DELL EMC S4148T-ON (336 W / 48 ports) [57].

Table 4.3: Considered energy consumption model and parameters of the system (Part 2).

	Symbol	Value	Unit	Ref.
<b>Parameter</b>				
Coherence time	$\tau_c$	200	symbols	
Pilot time	$\tau_p$	$K/F = 12$	symbols	
RF sampling rate	$f_s$	600	MHz	[58]
Base-band sampling rate	$f_{BB}$	20	MHz	
Max. PA efficiency	$\eta_{\max}$	0.34*		[59]
Max. transmit power	$P_{t,\max}$	3	W	[59]
	$E_{mac}$	3.1	pJ/oper	[46]
	$E_{sram}$	5	pJ/oper	[46]
	$E_{dram}$	640	pJ/oper	[46]
Energy overhead	$\zeta$	1.2		
FoM (DAC)	$FoM_W$	34.4	fJ/step	[58]
	$\alpha$	10%		[46]
	$\gamma$	1%		[46]
Num. of bits	$b$	12		
Num. of served users	$K$			
Num. of antennas per CSP	$M$			

\* obtained by finding the PAE at  $P_{t,\max}$  in [59].

**Power Amplifier** The CSPs feature a PA per RF chain. The power consumption of the PA is given as

$$P_{\text{PA}} = \frac{1}{\eta_{\text{max}}} \left( \frac{P_{\text{t,max}}}{P_{\text{t}}} \right)^{\beta} P_{\text{t}}, \quad (4.16)$$

where  $\eta_{\text{max}} \in (0, 1]$  is the PAE achieved when the transmit power is  $P_{\text{t}} = P_{\text{t,max}}$ . This parameter and  $\beta$  are PA-dependent, where a typical value for  $\beta$  would be between 0.4 and 0.5 [54].<sup>1</sup>

**Sampling and Processing** The energy model of the CSP considered in this work also encompasses the energy consumption associated with sampling and processing (Table 4.2 and Table 4.3).

A 12-bit ADC sampling at 600 MHz is utilized, which is active during the pilot phase. These samples are down-sampled and processed for channel estimation. A digital-to-analog converter (DAC) with the identical parameters is used during the downlink data transmission. The respective energy consumption depends on the energy consumption per arithmetic operation. Here, we assume a two-input multiplier as the typical arithmetic operation, where every operation requires retrieving operands from storage elements and storing them, e.g., register files, on-chip static random-access memory (SRAM), or off-chip dynamic random-access memory (DRAM).

**Energy Model** The full energy model for the ECSPs and CSPs for one coherence block becomes,

$$E_{\text{ECSP}} = (P_{\text{eth}} + P_{\text{sync}}) \frac{\tau_c}{f_{\text{BB}}} \quad (4.17)$$

$$E_{\text{CSP}} = E_{\text{LP}} + E_{\text{CE}} + E_{\text{PA}} + E_{\text{ECSP}} + E_{\text{DAC}}. \quad (4.18)$$

Details are summarized in Table 4.2 and Table 4.3.

#### 4.3.1.1 System Model

Let  $\mathcal{S} = \{1, \dots, S\}$  and  $\bar{\mathcal{S}} = \{1, \dots, \bar{S}\}$  denote the sets of CSPs and ECSPs, respectively, where  $S = |\mathcal{S}|$  and  $\bar{S} = |\bar{\mathcal{S}}|$ . Predefined sets of CSPs are connected to each ECSP, forming disjoint sets. We let  $\mathcal{S}(\bar{s})$  denote the set of CSPs connected to ECSP  $\bar{s}$ . We have  $\mathcal{S}(\bar{s}) \cap \mathcal{S}(\bar{s}') = \emptyset$  for  $\bar{s} \neq \bar{s}'$  and  $\bigcup_{\bar{s} \in \bar{\mathcal{S}}} \mathcal{S}(\bar{s}) = \mathcal{S}$ . We assume that each UE belongs to one federation and is served jointly by the CSPs of that federation. For a given snapshot, suppose that there are  $K$  UEs connected to the network. The set of UEs is denoted by  $\mathcal{K} = \{1, \dots, K\}$ , where  $K = |\mathcal{K}|$ . The maximum possible number of federations for joint transmission is  $F$  and the set of federations is denoted by  $\mathcal{F} = \{1, \dots, F\}$ , where  $F = |\mathcal{F}|$ .  $|\mathcal{F}|$  should be large enough that there will be enough federations to accommodate all UEs and CSPs, and, in general, not all federations  $f \in \mathcal{F}$  need to be used. A simple upper bound for  $|\mathcal{F}|$  is the number of UEs, since one will never need more federations than would be enough to place each UE in its own federation, but in practice  $|\mathcal{F}|$  can be much smaller than this.

We assume a block fading channel model, where the channels take independent realizations in each coherence block. We let  $\tau_p$  denote the number of mutually orthogonal pilot sequences. To eliminate pilot contamination, each joint transmission federation can only serve up to  $\tau_p$  UEs so that they can share mutually orthogonal pilot sequences. Let  $\tau_c > \tau_p$  denote the number of

<sup>1</sup>In this work,  $\beta$  is set to 0.5 to facilitate optimization with an objective function involving Euclidean norm.



channel uses in each coherence block. The payload data is transmitted using  $\tau_c - \tau_p$  channel uses in each coherence block.

We let  $M$  denote the number of antennas per CSP. We will assume uncorrelated Rayleigh fading and let  $h_{k,s,m} \in \mathcal{N}_{\mathbb{C}}(0, \beta_{k,s})$  denote the channel from the  $m$ th antenna of CSP  $s$  to UE  $k$ , where the large-scale fading channel coefficient is  $\beta_{k,s} > 0$ . We let  $\rho_p$  denote the normalized signal-to-noise ratio (SNR) of each pilot symbol. The channels  $h_{k,s,m}$  can be estimated using the minimum mean square error (MMSE) estimator [62] and the variance of the MMSE estimate of the channels  $h_{k,s,m}$  can be computed as

$$\gamma_{k,s} = \frac{\tau_p \rho_p \beta_{k,s}^2}{\tau_p \rho_p \beta_{k,s} + 1}. \quad (4.19)$$

We let  $x_k^f \in \{0, 1\}$  denote the binary variable representing whether UE  $k$  belongs to federation  $f$  or not, i.e.,  $x_k^f = 1$  if UE  $k$  belongs to federation  $f$  and  $x_k^f = 0$  otherwise. Similarly,  $y_s^f \in \{0, 1\}$  denotes whether CSP  $s$  belongs to federation  $f$  or not. Note that each CSP and each UE can only belong to one federation, i.e.,  $\sum_{f \in \mathcal{F}} y_s^f \leq 1, \forall s$  and  $\sum_{f \in \mathcal{F}} x_k^f = 1, \forall k$ .

Different sets of federations use orthogonal time-frequency resources so that there is no inter-federation interference. We assume that CSP  $s$  uses the total transmit power of  $(\rho_s^f)^2$  if it belongs to federation  $f$  and active, so we have the relation

$$\rho_s^f \leq \sqrt{P_{\max} y_s^f}. \quad (4.20)$$

Under this scenario, an achievable downlink data rate of UE  $k$  belonging to one of the federations in  $\mathcal{F}$  using maximum ratio transmission (MRT) precoding and equal power allocation with  $(\rho_s^f)^2 / \tau_p$  can be derived from [62, Corol. 6.3 and 6.4] as<sup>2</sup>

$$R_k^{\text{dl}} = \frac{\tau_c - \tau_p}{\tau_c} \times \log_2 \left( 1 + \frac{M/\tau_p \left( \sum_{f \in \mathcal{F}} \sum_{s \in \mathcal{S}} x_k^f \rho_s^f \sqrt{\gamma_{k,s}} \right)^2}{\sum_{f \in \mathcal{F}} \sum_{s \in \mathcal{S}} x_k^f (\rho_s^f)^2 \beta_{k,s} + \sigma^2} \right) \quad (4.21)$$

where  $\sigma^2$  is the noise variance at the receiver of each UE  $k$ .

#### 4.3.1.2 Problem Formulation

The overall aim is to minimize total energy consumption under the UE data rate constraints and federation assignment rules.

<sup>2</sup>The MRT precoding and equal power allocation enable to express the highly combinatorial problem in a more manageable form.

$$\begin{aligned}
& \underset{\{x_k^f, y_s^f, z_{\bar{s}}, \rho_s^f\}}{\text{minimize}} \quad \bar{E}_{\text{CSP}} \sum_{s \in \mathcal{S}} \sum_{f \in \mathcal{F}} y_s^f + E_{\text{ECSP}} \sum_{\bar{s} \in \bar{\mathcal{S}}} z_{\bar{s}} \\
& \quad + (\tau_c - \tau_p) f_{\text{BB}}^{-1} \frac{\sqrt{P_{t, \max}}}{\eta_{\max}} \sum_{s \in \mathcal{S}} \sqrt{\sum_{f \in \mathcal{F}} (\rho_s^f)^2}
\end{aligned} \tag{4.22a}$$

subject to:

$$\begin{aligned}
& x_k^f M / \tau_p \left( \sum_{s \in \mathcal{S}} \rho_s^f \sqrt{\gamma_{k,s}} \right)^2 \geq x_k^f \text{SINR}_k^{\text{thr}} \\
& \quad \times \left( \sum_{s \in \mathcal{S}} (\rho_s^f)^2 \beta_{k,s} + \sigma^2 \right), \quad \forall k \in \mathcal{K}, \forall f \in \mathcal{F}
\end{aligned} \tag{4.22b}$$

$$\rho_s^f \leq \sqrt{P_{\max}} y_s^f, \quad \forall s \in \mathcal{S}, \forall f \in \mathcal{F} \tag{4.22c}$$

$$\sum_{f \in \mathcal{F}} y_s^f \leq z_{\bar{s}}, \quad \forall s \in \mathcal{S}(\bar{s}), \forall \bar{s} \in \bar{\mathcal{S}} \tag{4.22d}$$

$$\sum_{f \in \mathcal{F}} x_k^f = 1, \quad \forall k \in \mathcal{K} \tag{4.22e}$$

$$\sum_{k \in \mathcal{K}} x_k^f \leq \tau_p, \quad \forall f \in \mathcal{F} \tag{4.22f}$$

$$x_k^f \in \{0, 1\}, \quad \forall k \in \mathcal{K}, \forall f \in \mathcal{F} \tag{4.22g}$$

$$y_s^f \in \{0, 1\}, \quad \forall s \in \mathcal{S}, \forall f \in \mathcal{F} \tag{4.22h}$$

$$z_{\bar{s}} \in \{0, 1\}, \quad \forall \bar{s} \in \bar{\mathcal{S}} \tag{4.22i}$$

where  $\bar{E}_{\text{CSP}} = E_{\text{CSP}} - E_{\text{PA}}$ , the objective function in (4.22a) is the total energy consumption per coherence block and  $\sqrt{\sum_{f \in \mathcal{F}} (\rho_s^f)^2}$  is used in place of  $\sqrt{P_t}$  in (4.16). The SINR constraint for each UE is given in (4.22b) and the relation between  $\rho_s^f$  and  $y_s^f$  from (4.20) is set in the constraint (4.22c). The constraints in (4.22d) ensure that ECSP  $\bar{s}$  is activated ( $z_{\bar{s}} = 1$ ) if at least one of the CSPs connected to it is active. These constraints also guarantee that each active CSP belongs to only one federation, i.e.,  $\sum_{f \in \mathcal{F}} y_s^f \leq 1$ . Similarly, the constraints in (4.22e) limit the number of federations each UE connects to one. To allow for mutually orthogonal pilot sequences in each federation, the number of maximum UEs in each federation is restricted by  $\tau_p$  in (4.22f). Finally, the constraints in (4.22g)-(4.22i) represent binary constraints.

### 4.3.1.3 Algorithm

A *divide-and-conquer* heuristic based on an *alternating minimization* scheme is employed. For more details, consult [52]. The idea is to alternate the solution of two subproblems; in particular, for each iteration  $\ell \in \{1, 2, \dots\}$ , we perform the following:

1. *Power allocation with fixed assignment*: fixing the binary variables  $\{x_k^f, y_s^f, z_{\bar{s}}\}$ , we solve for the continuous optimization variables  $\{\rho_s^f, \epsilon_s^f, \tilde{\epsilon}_k^f\}$ . The resulting problem is a convex programming problem since the constraints can be expressed as second-order cone constraints and the functions in the objective and the other constraints are convex.

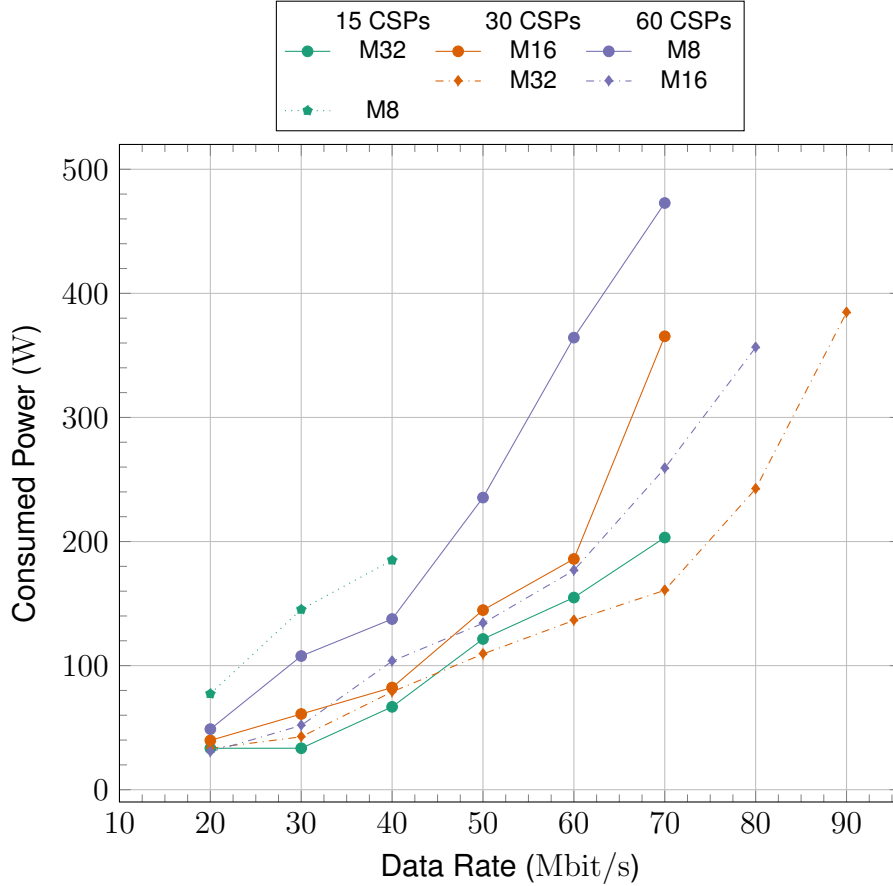


Figure 4.2: Total power consumption in terms of data rate for different numbers of CSPs and antennas. Each row in the legend corresponds with the same number of total antennas.

2. *Federation and CSP/ECSP assignment with fixed power*: fixing  $\{\rho_s^f\}$  to the solution obtained in 1) is now solved for the binary variables  $\{x_k^f, y_s^f, z_{\bar{s}}\}$  and slack variables  $\{\epsilon_s^f, \tilde{\epsilon}_k^f\}$ . The problem in this case is a mixed-integer linear programming problem, and can be solved by branch-and-bound-type algorithms.

The proposed algorithm continues alternating between 1) and 2) until a termination condition is reached.

#### 4.3.1.4 Evaluation in an Industrial Factory Environment

The proposed algorithm is evaluated in an industrial environment. The carrier frequency is 3 GHz. The path loss, i.e., large-scale fading, is simulated based on the channel models proposed by ET SI and 3GPP [63], more specially the *indoor factory (sparse clutter, high base station)* is used. The probability that a UE is in line-of-sight (LoS) follows the model proposed in [63]. A fixed number of ECSPs is selected, i.e., 5 ECSPs.

The simulated industrial factory hall measures 12 meters in width, 20 meters in length, and 10 meters in height. The CSP units are evenly distributed and integrated into the ceiling. Additionally,  $K = 24$  UEs are simulated at random locations within the hall.

In Figure 4.2, we set the number of federations to  $F = 2$  and the pilot channel uses to  $\tau_p = K/F = 12$ , resulting in UEs being forced to be in two federations. We consider several numbers of CSPs and antennas per CSPs,  $M$ . If the problem is infeasible, no point is shown in the figure

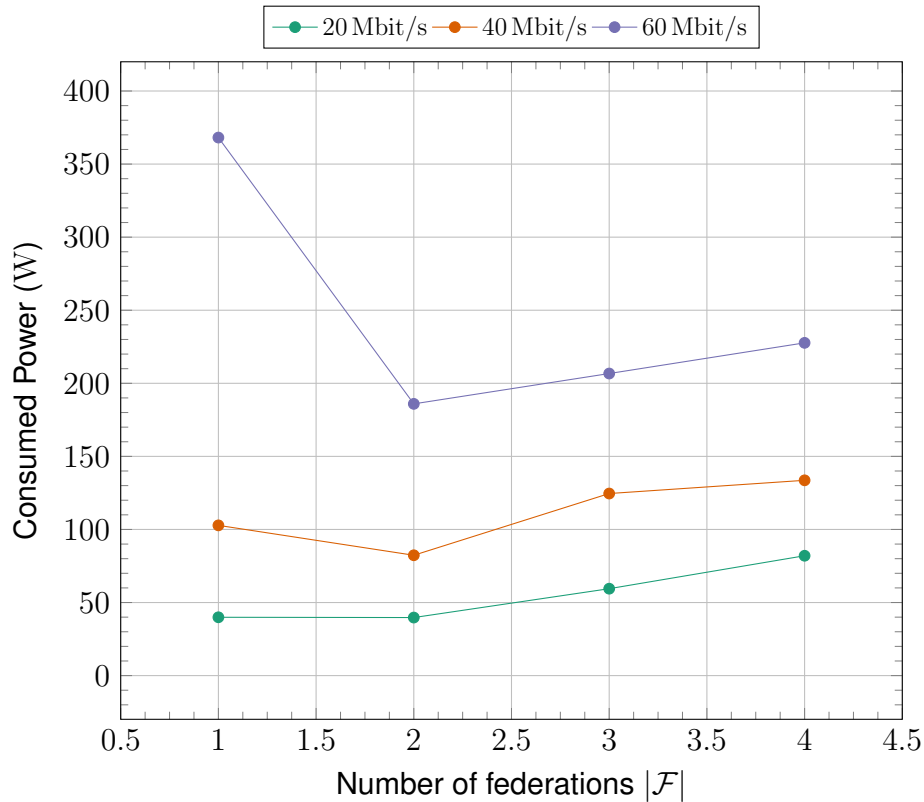


Figure 4.3: Power consumption in terms of number of federations for different rate requirements.

for the corresponding data rate requirement. For example, 15 CSPs with  $M = 8$  antennas cannot provide 50 Mbit/s and more. When we increase the number of antennas per CSP for a given number of CSPs, we can both improve the feasibility and reduce power consumption. Moreover, this figure showcases that less distributed CF-mMIMO structure provides better energy saving. This effect was not observed in original works on cell-free massive MIMO, as they only focus on radio power consumption. However, since the cost per CSP is much larger than the number of antennas, we observe this effect.

In Figure 4.3, we set  $\tau_p = K/F$  and vary  $F$ . There are  $S = 30$  CSPs with  $M = 16$ . We observe that  $F = 2$  federations are optimal for power consumption when the data rate requirement is low. As the data rate requirement increases, the advantages of using  $F = 2$  federations for energy savings become more pronounced. Figure 4.3 illustrates the versatile nature of the proposed system, showcasing a significant reduction in power consumption when the requested downlink data transfer rate is low. However, the system has the capability to scale up its performance as needed, depending on the real-time load.

This study highlights that in certain scenarios, a co-located deployment exhibits energy advantages over a cell-free (CF) network when considering the energy consumption of the infrastructure. This implies that for a limited number of users and a small indoor scenario, it becomes imperative that the energy requirements of the CSPs should be reduced in order for it to become a sustainable system.

### 4.3.2 Optimizing the WPT considering the transmit consumption

WPT using distributed MIMO systems is gaining traction due to its potential to eliminate batteries in low-power devices like ESLs. This work done in REINDEER and published in [64] focuses on optimizing the energy delivery to ERs such as ESLs, minimizing the total system transmit power. The approach prioritizes efficient energy delivery over continuous power maximization, tailoring energy provision to the requirements of each ER.

### 4.3.3 Key Contributions

This study investigates the impact of distributed precoding techniques in coherent and non-coherent system configurations. The primary contributions are:

- Development of optimal precoding schemes for both synchronized (coherent) and unsynchronized (non-coherent) systems.
- Numerical and experimental validation of energy delivery optimization using a testbed with 84 antennas.
- Insights into the performance improvements achieved by transitioning from non-coherent to coherent systems and increasing the number of antennas.

### 4.3.4 System Model

The system comprises multiple antennas distributed across ETs, which wirelessly charge ERs over specified time slots, as indicated in Figure 4.4. Energy is transferred using narrowband signals, optimized to meet the energy demands of ERs. Key assumptions include static channels over the transmission period and perfect CSI for coherent systems. For more details, we refer to [64].

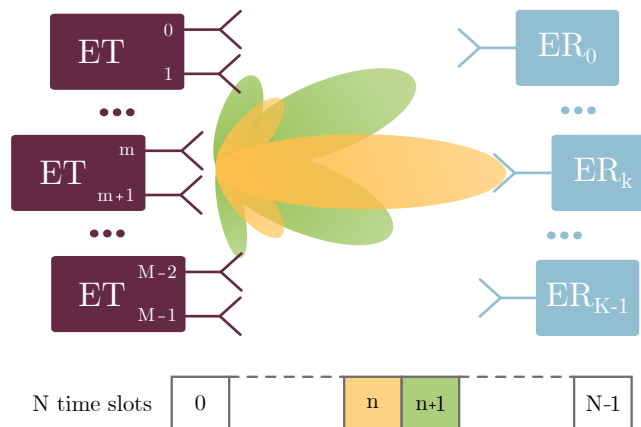



Figure 4.4: Illustration of a distributed WPT system, where several ETs transmit signals over  $M$  antennas to  $K$  ERs to charge them over  $N$  time slots. In this example, during slot  $n$  only ER  $k$  is targeted, while at  $n + 1$  ER<sub>0</sub> and ER <sub>$K-1$</sub>  is being charged.

### 4.3.5 Optimization Framework

Two optimization scenarios are explored:

1. **Non-Coherent System:** Assumes independent phase variations among signals, optimizing power allocation across antennas to meet ER energy requirements.
2. **Coherent System:** Leverages precise CSI and synchronization to use beamforming for targeted energy delivery, minimizing total transmit power.

The optimization ensures that each ER receives sufficient energy without exceeding system constraints. Numerical methods, including semidefinite programming, are employed to solve the formulated problems. The scripts are published in open-source [65] .

## 4.3.6 Evaluation and Results

### 4.3.6.1 Impact on increasing the number of antennas

Figure 4.5 illustrates the required total transmit power of the entire system relative to the number of antennas utilized.<sup>3</sup> It can be observed that the performance of the non-coherent system plateaus quickly, whereas the coherent system shows improvement with an increasing number of antennas. The performance of the non-coherent system levels off around 10 antennas, with the optimization consistently utilizing only approximately 10 antennas regardless of the total number available. This in contrast to the coherent system, which utilizes all available antennas. **The optimization problem favors sparsity in the spatial (antenna) domain in the non-coherent case, which is not the case in the coherent system, where all antennas are utilized.**

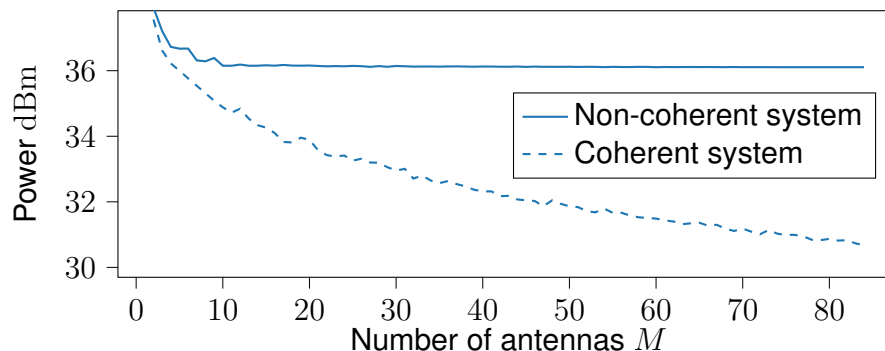
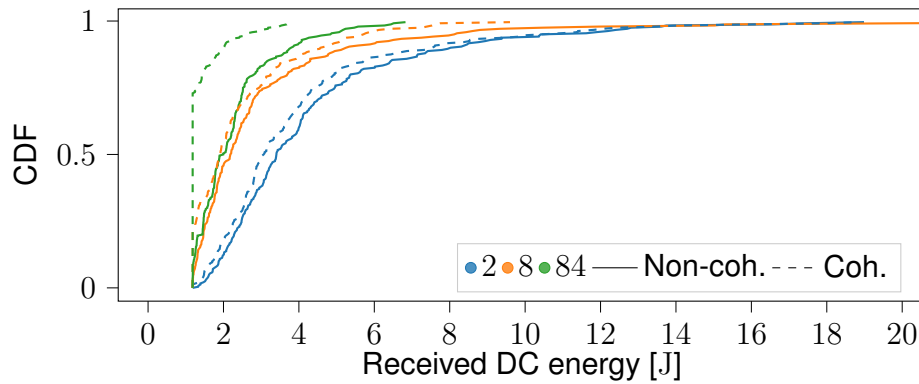


Figure 4.5: Total transmit power of all deployed antennas for the coherent and non-coherent system. Initially, with a limited number of antennas, both systems exhibit similar transmit power, when the number of antennas increases, the non-coherent system plateaus, whereas the coherent system continues to improve.

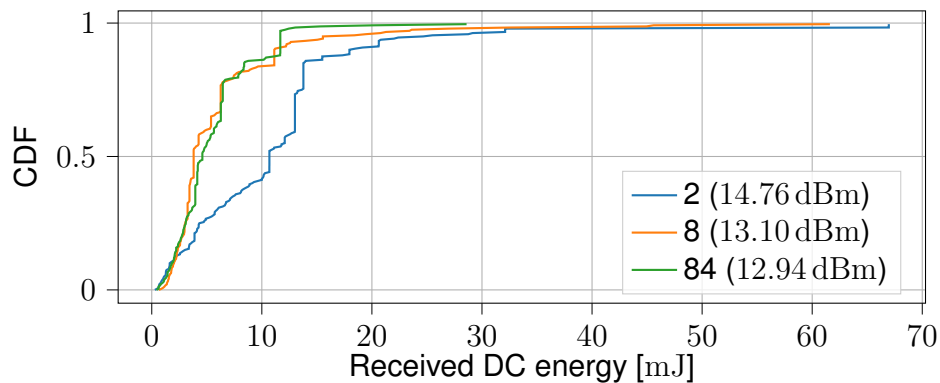
### 4.3.6.2 Distribution of harvested energy

In both systems, the accuracy of the targeted received DC power improves with having more antennas, as indicated by the CDF in Figure 4.6a. With increased number of antennas, i) the total transmit power is decreased, ii) the variance of received energy over all ESLs is decreased and iii) the maximum received DC energy is reduced. The coherent system outperforms the non-coherent system in aforementioned regards, while at the same time uses less transmit power in Figure 4.6a.

<sup>3</sup>The power values should be interpreted as if the system were transmitting continuously at that level over the full 12 h period, although this is not the actual case, see Figure 4.7.



(a) Numerical evaluation. CDF in the non-coherent (solid) and coherent (dashed) scenario.



(b) Experimental evaluation. Non-coherent measurements including the used total transmit power in brackets.

Figure 4.6: Simulation (a) and measurement-based (b) CDF of the received DC energy over the full 12-hour window for 2, 8 and 84 antennas.

#### 4.3.6.3 Effect of number of timeslots

In the non-coherent system, the solution keeps the same transmit power constant per antenna for all time slots and only uses a selection of the available antennas. This in contrast to the coherent, which utilizes only a few time slots and employs all antennas, as shown in Figure 4.7. **In contrast to the spatial domain, in the temporal domain, the optimization problem favors sparsity in the coherent case, while using all time slots in the non-coherent system.**

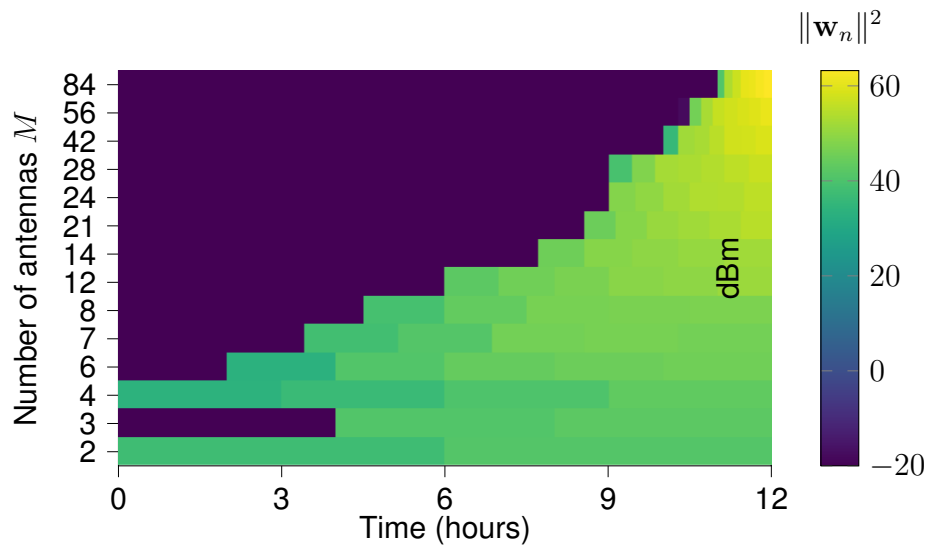


Figure 4.7: The used transmit powers (z-axis) over the full-time window (x-axis) for different number of available antennas (y-axis) in the coherent system.

### 4.3.7 Conclusion

This work demonstrates that increasing the number of antennas and adopting coherent precoding significantly enhances WPT efficiency. Coherent systems reduce energy overshoots and total energy consumption, aligning delivered energy with ER requirements. Despite this, the increased energy consumption and hardware complexity of the coherent system is not taken into account.



# Chapter 5

## Summary

This final deliverable from WP2 adds to the previous results reported on in REINDEER deliverables D2.1 [1], D2.2 [2], and D2.3 [3]. In particular, it puts into context studies performed at the end of the project, where a greater focus is put on RadioWeaves hardware for practical and more realistic scenarios. After setting the stage in the first two chapters, the main contributions are reported in chapters 3 and 4.

The importance of being able to deactivate parts of the infrastructure, or allow it to enter into low-power sleep modes, is described. Requirements/recommendations regarding both analog and digital parts of the RadioWeaves hardware are described, as well as an overview of options for synchronization across the infrastructure.

A particularly important key performance indicator (KPI) in the context of real deployments of a RadioWeaves infrastructure is the energy efficiency. In this deliverable we analyze energy efficiency, establishing energy consumption models both for analog and digital parts of a RadioWeaves infrastructure. A RadioWeaves communication case study based on these energy models show that, under the assumptions made and in certain scenarios, a co-located deployment exhibits energy advantages over a cell-free (CF) network. In particular, for small indoor scenarios with a limited number of users, the energy requirement of the CSPs are highly critical for the sustainability. Likewise, a RadioWeaves power transfer case study show that, under the assumptions made, how non-coherent and coherent operation of WPT differ in their performance. Both approaches lead to lower requirement on transmitted power with increasing number of antennas, but coherent operation outperforms non-coherent in several measures as well as using less transmit power.

# Bibliography


- [1] O. Edfors, R. Brazil, H. Petautschnig, G. Callebaut, T. Feys, L. V. der Perre, E. G. Larsson, O. Edfors, E. Fitzgerald, L. Liu, J. R. Sanchez, W. Tärneberg, P. Frenger, B. Deutschmann, T. Wilding, and K. Witrissal, “Initial assessment of architectures and hardware resources for a RadioWeaves infrastructure, Reindeer deliverable D2.1,” REINDEER project, Deliverable ICT-52-2020 / D2.1, Jan. 2022. [Online]. Available: <https://doi.org/10.5281/zenodo.5938909>
- [2] REINDEER project, “Evaluation of the distribution of processing across infrastructure and associated requirements on back-haul and synchronization,” Deliverable ICT-52-2020 / D2.3, 2023.
- [3] —, “Hardware requirements to support energy transfer to energy-neutral nodes,” Deliverable ICT-52-2020 / D2.3, 2023.
- [4] G. Callebaut, J. Van Mulders, B. Cox, L. Van der Perre, L. De Strycker, and F. Rottenberg, “How to perform distributed precoding to wirelessly power shelf labels: Signal processing and measurements,” in *2024 IEEE 25th International Workshop on Signal Processing Advances in Wireless Communications (SPAWC) (IEEE SPAWC 2024)*, Lucca, Italy, Sep. 2024, p. 4.97.
- [5] J. F. Esteban and M. Truskaller, “Use case-driven specifications and technical requirements and initial channel model,” REINDEER project, Deliverable ICT-52-2020 / D1.1, Sep 2021.
- [6] E. G. Larsson, O. Edfors, F. Tufvesson, and T. L. Marzetta, “Massive MIMO for next generation wireless systems,” *IEEE Communications Magazine*, vol. 52, no. 2, pp. 186–195, 2014.
- [7] Y. Li, C. Tao, G. Seco-Granados, A. Mezghani, A. L. Swindlehurst, and L. Liu, “Channel Estimation and Performance Analysis of One-Bit Massive MIMO Systems,” *IEEE Transactions on Signal Processing*, vol. 65, no. 15, pp. 4075–4089, 2017.
- [8] C. Mollén, J. Choi, E. G. Larsson, and R. W. Heath, “Uplink Performance of Wideband Massive MIMO With One-Bit ADCs,” *IEEE Transactions on Wireless Communications*, vol. 16, no. 1, pp. 87–100, 2017.
- [9] M. Sarajlić, L. Liu, and O. Edfors, “When Are Low Resolution ADCs Energy Efficient in Massive MIMO?” *IEEE Access*, vol. 5, pp. 14 837–14 853, 2017.
- [10] *Data sheet BTS6403U – Wideband high gain high linearity pre-driver amplifier 2.3 GHz - 4.2 GHz*, NXP, 5 2023. [Online]. Available: <https://www.nxp.com/docs/en/data-sheet/BTS6403U.pdf>
- [11] P. Cruz, N. B. Carvalho, and K. A. Remley, “Designing and testing software-defined radios,” *IEEE Microwave magazine*, vol. 11, no. 4, pp. 83–94, 2010.

- [12] U. M. Dean Banerjee, Mohan Rudrappa and T. I. Ajeet Pal, “Improve phase noise by down-converting the vco frequency,” <https://www.planetanalog.com/improve-phase-noise-by-down-converting-the-vco-frequency>, 2021, accessed: 2024-08-29.
- [13] Analog Devices, “D9361 reference manual,” Analog Devices, Tech. Rep. UG-570, 2014, reference manual.
- [14] J. Van Mulders, B. Cox, B. J. B. Deutschmann, G. Callebaut, L. De Strycker, and L. Van der Perre, “Keeping Energy-Neutral devices operational: a coherent massive beamforming approach,” in *2024 IEEE 25th International Workshop on Signal Processing Advances in Wireless Communications (SPAWC) (IEEE SPAWC 2024)*, Lucca, Italy, Sep. 2024, p. 4.97.
- [15] A. Paulraj, R. Nabar, and D. Gore, *Introduction to Space-Time Wireless Communications*, 1st ed. USA: Cambridge University Press, 2008.
- [16] Z. H. Shaik, S. S. Thoota, E. Björnson, and E. G. Larsson, “Resource efficient over-the-air fronthaul signaling for uplink cell-free massive MIMO systems,” in *ICC 2024 - IEEE International Conference on Communications*, 2024, pp. 5039–5044.
- [17] J. Vidal Alegria, J. Rodriguez Sanchez, F. Rusek, L. Liu, and O. Edfors, “Decentralized equalizer construction for large intelligent surfaces,” in *2019 IEEE 90th Vehicular Technology Conference (VTC2019-Fall)*, 2019, pp. 1–6.
- [18] G. Callebaut, L. Liu, T. Eriksson, L. Van der Perre, O. Edfors, and C. Fager, “6G Radio Testbeds: Requirements, Trends, and Approaches,” *IEEE Microwave Magazine*, vol. 25, no. 4, pp. 14–31, 2024.
- [19] A. Bourdoux, B. Come, and N. Khaled, “Non-reciprocal transceivers in OFDM/SDMA systems: Impact and mitigation,” in *Proceedings - 2003 IEEE Radio and Wireless Conference, RAWCON 2003*. Institute of Electrical and Electronics Engineers Inc., 2003, pp. 183–186.
- [20] F. Kaltenberger, H. Jiang, M. Guillaud, and R. Knopp, “Relative channel reciprocity calibration in MIMO/TDD systems,” in *2010 Future Network and Mobile Summit*. IEEE, 2010, pp. 1–10.
- [21] C. Shepard, H. Yu, N. Anand, L. E. Li, T. Marzetta, R. Yang, and L. Zhong, “Argos: Practical many-antenna base stations,” in *Proceedings of the Annual International Conference on Mobile Computing and Networking, MOBICOM*. New York, New York, USA: ACM Press, 2012, pp. 53–64.
- [22] R. Rogalin, O. Y. Bursalioglu, H. Papadopoulos, G. Caire, A. F. Molisch, A. Michaloliakos, V. Balan, and K. Psounis, “Scalable synchronization and reciprocity calibration for distributed multiuser MIMO,” *IEEE transactions on wireless communications*, vol. 13, no. 4, pp. 1815–1831, 2014.
- [23] J. Vieira, F. Rusek, and F. Tufvesson, “Reciprocity calibration methods for massive MIMO based on antenna coupling,” in *2014 IEEE Global Communications Conference, GLOBECOM 2014*. Institute of Electrical and Electronics Engineers Inc., feb 2014, pp. 3708–3712.
- [24] R. N. Braithwaite, “Digital Predistortion of a RF Power Amplifier using a Remote Closed Loop Estimator,” in *2020 IEEE Topical Conference on RF/Microwave Power Amplifiers for Radio and Wireless Applications, PAWR 2020*. Institute of Electrical and Electronics Engineers Inc., jan 2020, pp. 42–45.

- [25] R. Mudumbai, D. R. Brown, U. Madhow, and H. V. Poor, "Distributed Transmit Beamforming : Challenges and Recent Progress," *IEEE Communications Magazine*, vol. 47, no. 2, pp. 102–110, 2009.
- [26] A. A. Nasir, S. Durrani, H. Mehrpouyan, S. D. Blostein, and R. A. Kennedy, "REVIEW Open Access Timing and carrier synchronization in wireless communication systems: a survey and classification of research in the last 5 years," *EURASIP Journal on Wireless Communications and Networking*, vol. 2016, p. 180, 2016.
- [27] "Techtile—open 6g r&d testbed for communication, positioning, sensing, wpt and federated learning."
- [28] P. B. Papazian, C. Gentile, K. A. Remley, J. Senic, and N. Golmie, "A Radio Channel Sounder for Mobile Millimeter-Wave Communications: System Implementation and Measurement Assessment," *IEEE Transactions on Microwave Theory and Techniques*, vol. 64, no. 9, pp. 2924–2932, 2016.
- [29] J. Breen, A. Buffmire, J. Duerig, K. Dutt, E. Eide, M. Hibler, D. Johnson, S. K. Kasera, E. Lewis, D. Maas, A. Orange, N. Patwari, D. Reading, R. Ricci, D. Schurig, L. B. Stoller, J. Van der Merwe, K. Webb, and G. Wong, "POWDER: Platform for Open Wireless Data-driven Experimental Research," in *Proceedings of the 14th International Workshop on Wireless Network Testbeds, Experimental Evaluation and Characterization (WiNTECH)*, Sep. 2020. [Online]. Available: <https://www.flux.utah.edu/paper/breen-wintech20>
- [30] M. H. Lee, M. C. Ha, H. S. Yoon, C. W. Yun, C. W. Yu, and K. W. Choi, "Demo: SDR Implementation of a Fully Distributed Cell-Free MIMO System," in *2022 IEEE International Conference on Communications Workshops (ICC Workshops)*, 2022, pp. 1–2.
- [31] Y. Cao, Z. Zhang, X. Xia, P. Xin, D. Liu, K. Zheng, M. Lou, J. Jin, Q. Wang, D. Wang, Y. Huang, X. You, and J. Wang, "From ORAN to Cell-Free RAN: Architecture, Performance Analysis, Testbeds and Trials," 2023. [Online]. Available: <https://arxiv.org/abs/2301.12804>
- [32] D. Wang, C. Zhang, Y. Du, J. Zhao, M. Jiang, and X. You, "Implementation of a Cloud-Based Cell-Free Distributed Massive MIMO System," *IEEE Communications Magazine*, vol. 58, no. 8, pp. 61–67, 2020.
- [33] M. M. Rahman, H. E. Baidoo-Williams, R. Mudumbai, and S. Dasgupta, "Fully wireless implementation of distributed beamforming on a software-defined radio platform," in *Proceedings of the 11th international conference on Information Processing in Sensor Networks*, 2012, pp. 305–316.
- [34] L. Breyne, G. Torfs, X. Yin, P. Demeester, and J. Bauwelinck, "Comparison between analog radio-over-fiber and sigma delta modulated radio-over-fiber," *IEEE Photonics Technology Letters*, vol. 29, no. 21, pp. 1808–1811, 2017.
- [35] M. M. Rahman, S. Dasgupta, and R. Mudumbai, "A distributed consensus approach to synchronization of RF signals," in *IEEE Statistical Signal Processing Workshop*. IEEE, 2012, pp. 281–284.
- [36] S. Rommel, D. Dodane, E. Grivas, B. Cimoli, J. Bourderionnet, G. Feugnet, A. Morales, E. Pikasis, C. Roeloffzen, P. van Dijk *et al.*, "Towards a scaleable 5G fronthaul: Analog radio-over-fiber and space division multiplexing," *Journal of Lightwave Technology*, vol. 38, no. 19, pp. 5412–5422, 2020.

- [37] A. Moerman, J. Van Kerrebrouck, O. Caytan, I. L. de Paula, L. Bogaert, G. Torfs, P. Demeester, H. Rogier, and S. Lemey, "Beyond 5G Without Obstacles: mmWave-over-Fiber Distributed Antenna Systems," *IEEE Communications Magazine*, vol. 60, no. 1, pp. 27–33, 2022.
- [38] L. M. Pessoa, J. S. Tavares, D. Coelho, and H. M. Salgado, "Experimental evaluation of a digitized fiber-wireless system employing sigma delta modulation," *Optics Express*, vol. 22, no. 14, pp. 17 508–17 523, Jul 2014.
- [39] C.-Y. Wu, H. Li, O. Caytan, J. Van Kerrebrouck, L. Breyne, J. Bauwelinck, P. Demeester, and G. Torfs, "Distributed multi-user MIMO transmission using real-time sigma-delta-over-fiber for next generation fronthaul interface," *Journal of Lightwave Technology*, vol. 38, no. 4, pp. 705–713, 2019.
- [40] I. C. Sezgin, M. Dahlgren, T. Eriksson, M. Coldrey, C. Larsson, J. Gustavsson, and C. Fager, "A Low-Complexity Distributed-MIMO Testbed Based on High-Speed Sigma-Delta-Over-Fiber," *IEEE Transactions on Microwave Theory and Techniques*, vol. 67, no. 7, pp. 2861–2872, 2019.
- [41] T. Bigler, A. Treytl, D. Loschenbrand, and T. Zemen, "High Accuracy Synchronization for Distributed Massive MIMO using White Rabbit," *IEEE International Symposium on Precision Clock Synchronization for Measurement, Control, and Communication, ISPCS*, vol. 2018-September, nov 2018.
- [42] L. Breyne, G. Torfs, X. Yin, P. Demeester, and J. Bauwelinck, "Comparison between analog radio-over-fiber and sigma delta modulated radio-over-fiber," *IEEE Photonics Technology Letters*, vol. 29, no. 21, pp. 1808–1811, 2017.
- [43] F. Quitin, U. Madhow, M. M. U. Rahman, and R. Mudumbai, "Demonstrating distributed transmit beamforming with software-defined radios," in *IEEE International Symposium on a World of Wireless, Mobile and Multimedia Networks (WoWMoM)*, 2012, pp. 1–3.
- [44] S. Muneer, L. Liu, O. Edfors, H. Sjöland, and L. V. der Petre, "Handling pa nonlinearity in massive mimo: What are the tradeoffs between system capacity and power consumption," in *2020 54th Asilomar Conference on Signals, Systems, and Computers*, 2020, pp. 974–978.
- [45] M. Sarajlić, L. Liu, and O. Edfors, "When Are Low Resolution ADCs Energy Efficient in Massive MIMO?" *IEEE Access*, vol. 5, pp. 14 837–14 853, 2017.
- [46] S. Han, X. Liu, H. Mao, J. Pu, A. Pedram, M. A. Horowitz, and W. J. Dally, "EIE: Efficient interference engine on compressed deep neural network," *ACM SIGARCH Computer Architecture News*, vol. 44, no. 3, pp. 243–254, 2016.
- [47] H. Okuhara, A. Elnaqib, D. Rossi, A. Di Mauro, P. Mayer, P. Palestri, and L. Benini, "An energy-efficient low-voltage swing transceiver for mw-range iot end-nodes," in *2020 IEEE International Symposium on Circuits and Systems (ISCAS)*, 2020, pp. 1–5.
- [48] J. L. Wei, D. G. Cunningham, R. V. Penty, and I. H. White, "Study of 100 gigabit ethernet using carrierless amplitude/phase modulation and optical ofdm," *Journal of Lightwave Technology*, vol. 31, no. 9, pp. 1367–1373, 2013.
- [49] S. Aleksic, "Power efficiency of 40 gbit/s and 100 gbit/s optical ethernet," in *2009 11th International Conference on Transparent Optical Networks*, 2009, pp. 1–1.

- [50] “White rabbit node reference design,” <https://ohwr.org/projects/white-rabbit/wiki/WRReferenceDesign>, accessed: 2021-11-26.
- [51] M. Attari, L. Ferreira, L. Liu, and S. Malkowsky, “An Application Specific Vector Processor for Efficient Massive MIMO Processing,” *IEEE Transactions on Circuits and Systems I: Regular Papers*, vol. 69, no. 9, pp. 3804–3815, 2022.
- [52] Ö. T. Demir, L. Mendez-Monsanto Suarez, N. Bastianello, E. Fitzgerald, and G. Callebaut, “Energy Reduction in Cell-Free Massive MIMO Through Fine-Grained Resource Management,” in *2024 European Conference on Networks and Communications & 6G Summit (EuCNC/6G Summit): Physical Layer and Fundamentals (PHY) (2024 EuCNC & 6G Summit - PHY)*, Antwerp, Belgium, Jun. 2024, p. 5.93.
- [53] L. Liu, G. Callebaut, J. V. Mulders, B. Cox, L. V. der Perre, E. Peschiera, X. Li, C. Nelson, W. T. Örneberg, J. V. Alegría, O. Edfors, S. Willhammar, Y. Xu, B. J. B. Deutschmann, T. Wilding, K. Witrisal, K. Deforche, U. Mühlmann, and S. S. Thoota, “Validation of concepts and experimental assessment of key technologies,” REINDEER project, Deliverable ICT-52-2020 / D5.3, 2024.
- [54] D. Persson, T. Eriksson, and E. G. Larsson, “Amplifier-Aware Multiple-Input Multiple-Output Power Allocation,” *IEEE Commun. Lett.*, vol. 17, no. 6, pp. 1112–1115, 2013.
- [55] D. Verenzuela, E. Björnson, and M. Matthaiou, “Hardware design and optimal ADC resolution for uplink massive MIMO systems,” in *Proc. IEEE Sensor Array Multichannel Signal Process. Workshop (SAM)*,, 2016, pp. 1–5.
- [56] “Wiki White Rabbit,” <https://ohwr.org/projects/white-rabbit/wiki/WRReferenceDesign#operating-power>.
- [57] G. Callebaut, J. V. Mulders, G. Ottoy, D. Delabie, B. Cox, N. Stevens, and L. V. d. Perre, “Techtile – Open 6G R&D Testbed for Communication, Positioning, Sensing, WPT and Federated Learning,” in *2022 Joint European Conference on Networks and Communications & 6G Summit (EuCNC/6G Summit)*, 2022, pp. 417–422.
- [58] J. Lagos, B. Hershberg, E. Martens, P. Wambacq, and J. Craninckx, “A Single-Channel, 600-MS/s, 12-b, Ringamp-Based Pipelined ADC in 28-nm CMOS,” *IEEE J. Solid-State Circuits*, vol. 54, no. 2, pp. 403–416, 2019.
- [59] *Datasheet QPA4501, 3 W, 28 V, 4.4 – 5.0 GHz GaN PA Module*, Qorvo, 9 2021. [Online]. Available: <https://www.qorvo.com/products/d/da006389>
- [60] M. Lipiński, T. Włostowski, J. Serrano, and P. Alvarez, “White rabbit: a PTP application for robust sub-nanosecond synchronization,” in *2011 IEEE International Symposium on Precision Clock Synchronization for Measurement, Control and Communication*, 2011, pp. 25–30.
- [61] G. Callebaut, L. Liu, T. Eriksson, L. Van der Perre, O. Edfors, and C. Fager, “6G Radio Testbeds: Requirements, Trends, and Approaches,” *IEEE Microw. Mag.*, vol. to appear, 2024.
- [62] Ö. T. Demir, E. Björnson, L. Sanguinetti *et al.*, “Foundations of user-centric cell-free massive MIMO,” *Foundations and Trends® in Signal Processing*, vol. 14, no. 3-4, pp. 162–472, 2021.
- [63] ETSI, “5G; Study on channel model for frequencies from 0.5 to 100 GHz (3GPP TR 38.901 version 16.1.0 Release 16),” ETSI, Tech. Rep. TR 138 901 - V16.1.0 - 5G, 2020.

- [64] G. Callebaut, J. Van Mulders, B. Cox, L. Van der Perre, L. De Strycker, and F. Rottenberg, "How to Perform Distributed Precoding to Wirelessly Power Shelf Labels: Signal Processing and Measurements," in *2024 IEEE 25th International Workshop on Signal Processing Advances in Wireless Communications (SPAWC) (IEEE SPAWC 2024)*, Lucca, Italy, Sep. 2024, p. 5.
- [65] G. Callebaut and F. Rottenberg, "How to Perform Distributed Precoding to Wirelessly Power Shelf Labels: Signal Processing and Measurements,"  <https://github.com/wavecore-research/distributed-WPT-SPAWC2024>, 2024.